

**CALCULATION OF THE MAGNETIC FIELD PENETRATION DEPTH
FOR HIGH- T_c CUPRATE SUPERCONDUCTORS BASED ON THE
INTERLAYER PAIR TUNNELING MODEL**

By

Melissa A. Castle

Honours B. Sc. (Physics) Brock University

A THESIS SUBMITTED IN PARTIAL FULFILLMENT OF
THE REQUIREMENTS FOR THE DEGREE OF
MASTER OF SCIENCE

in

THE FACULTY OF MATHEMATICS AND SCIENCE
DEPARTMENT OF PHYSICS

BROCK UNIVERSITY

September 1999

© Melissa A. Castle, 1999

In presenting this thesis in partial fulfilment of the requirements for an advanced degree at Brock University, I agree that the Library shall make it freely available for reference and study. I further agree that permission for extensive copying of this thesis for scholarly purposes may be granted by the head of my department or by his or her representatives. It is understood that copying or publication of this thesis for financial gain shall not be allowed without my written permission.

Department of Physics
Brock University
500 Glenridge Avenue
St. Catharines, Ontario
Canada L2S 3A1

Date:

Abstract

In this work, the magnetic field penetration depth for high- T_c cuprate superconductors is calculated using a recent Interlayer Pair Tunneling (ILPT) model proposed by Chakravarty, Sudbø, Anderson, and Strong [1] to explain high temperature superconductivity. This model involves a “hopping” of Cooper pairs between layers of the unit cell which acts to amplify the pairing mechanism within the planes themselves. Recent work has shown that this model can account reasonably well for the isotope effect and the dependence of T_c on nonmagnetic in-plane impurities [2], as well as the Knight shift curves [3] and the presence of a magnetic peak in the neutron scattering intensity [4]. In the latter case, Yin *et al.* emphasize that the pair tunneling must be the dominant pairing mechanism in the high- T_c cuprates in order to capture the features found in experiments.

The goal of this work is to determine whether or not the ILPT model can account for the experimental observations of the magnetic field penetration depth in $\text{YBa}_2\text{Cu}_3\text{O}_{7-x}$. Calculations are performed in the weak and strong coupling limits, and the effects of both small and large strengths of interlayer pair tunneling are investigated. Furthermore, as a follow up to the penetration depth calculations, both the neutron scattering intensity and the Knight shift are calculated within the ILPT formalism. The aim is to determine if the ILPT model can yield results consistent with experiments performed for these properties.

The results for all three thermodynamic properties considered are not consistent with the notion that the interlayer pair tunneling must be the dominate pairing mechanism in these high- T_c cuprate superconductors. Instead, it is found that reasonable agreement with experiments is obtained for small strengths of pair tunneling, and that large pair tunneling yields results which do not resemble those of the experiments.

Table of Contents

Abstract	ii
Acknowledgement	viii
1 INTRODUCTION	1
1.1 Structure of YBCO	2
1.2 Experimental Penetration Depth Data	3
1.3 Overview	5
2 THEORY	6
2.1 The Interlayer Pair Tunneling Model	6
2.2 Strong Coupling Form of the ILPT Model	9
2.2.1 Equations at the Critical Temperature	14
2.2.2 The Power Method	15
2.3 ILPT Model in the BCS Limit	16
2.4 The Magnetic Field Penetration Depth	17
2.4.1 Strong Coupling Limit	19
2.4.2 BCS Limit	21
2.5 Knight Shift	22
2.6 Magnetic Neutron Scattering Intensity	24
3 COMPUTING PROCEDURE	25
3.1 Summations in Momentum and Frequency Space	25

3.2	Strong Coupling Calculations	28
3.2.1	Penetration Depth Calculation	30
3.2.2	The Tetrahedron Method	31
3.3	BCS Calculations	35
4	NUMERICAL RESULTS AND DISCUSSION	37
4.1	BCS Limit	37
4.1.1	Penetration Depth (s-wave Symmetry)	38
4.1.2	Penetration Depth (d-wave Symmetry)	44
4.1.3	Knight Shift	58
4.1.4	Neutron Scattering Intensity	62
4.2	Strong Coupling Limit	67
5	CONCLUSIONS	78
	Bibliography	82

List of Figures

1.1	YBa ₂ Cu ₃ O ₇ unit cell	3
1.2	Experimental results for the penetration depth in YBa ₂ Cu ₃ O _{6.95}	4
2.1	The structure of $T_J(\mathbf{k})$	8
2.2	The magnetic field penetration depth $\lambda_L(T)$	19
3.1	The symmetry of the FBZ and the IW (shaded region).	27
3.2	The Tetrahedron Method: Division of triangles in the irreducible wedge.	32
3.3	The Tetrahedron Method: Energy contour crossing a single triangle i	34
4.1	Electronic density of states for the tight binding dispersion $\epsilon_{\mathbf{k}}$	38
4.2	The dependence of $1/\lambda^2(T)$ on temperature for several strengths of interlayer tunneling assuming s-wave BCS in-plane interaction.	40
4.3	Comparison of $1/\lambda^2(T)$ calculated using the tetrahedron method and direct \mathbf{k} space summation assuming s-wave BCS in-plane interaction.	41
4.4	The weighted density of states assuming s-wave BCS in-plane interaction with an interlayer tunneling strength of $T_J = 40meV$	43
4.5	The dependence of $1/\lambda^2(T)$ on temperature for several strengths of interlayer tunneling assuming d-wave BCS in-plane interaction.	45
4.6	The weighted density of states assuming d-wave BCS in-plane interaction with no interlayer pair tunneling.	46
4.7	The weighted density of states assuming d-wave BCS in-plane interaction with an interlayer tunneling strength of $T_J = 40meV$	47

4.8	The structure of $\phi(\mathbf{k})$ in the BCS limit assuming d-wave symmetry of the in-plane interaction. Here, $T = 0K$ and $T_J = 40meV$	48
4.9	The weighted density of states calculated assuming d-wave BCS in-plane interaction for two different lattice sizes with $T_J = 40meV$	49
4.10	The maximum of the gap assuming d-wave BCS in-plane interaction for several strengths of interlayer tunneling.	51
4.11	The structure of $\phi(\mathbf{k})$ in the BCS limit assuming d-wave symmetry of the in-plane interaction. Here, $T = 93K$ and $T_J = 40meV$	53
4.12	The structure of $\phi(\mathbf{k})$ in the BCS limit assuming d-wave symmetry of the in-plane interaction. Here, $T = 0K$ and $T_J = 0meV$	54
4.13	The structure of $\phi(\mathbf{k})$ in the BCS limit assuming d-wave symmetry of the in-plane interaction. Here, $T = 93K$ and $T_J = 0meV$	55
4.14	Comparison of $1/\lambda^2(T)$ calculated using the tetrahedron method and direct \mathbf{k} space summation assuming d-wave BCS in-plane interaction. . . .	56
4.15	Comparison of $1/\lambda^2(T)$ calculated using the tetrahedron method and direct \mathbf{k} space summation for a 512×512 lattice assuming d-wave BCS in-plane interaction and no interlayer pair tunneling.	57
4.16	The effect of lattice size on $1/\lambda^2(T)$ calculated with the tetrahedron method assuming d-wave BCS in-plane interaction.	59
4.17	The Knight shift calculated for $T_J = 43meV$ assuming s-wave BCS in-plane interaction.	60
4.18	The Knight shift calculated for several different strengths of pair tunneling assuming d-wave BCS in-plane interaction.	61
4.19	The magnetic neutron scattering intensity at $T = 0K$ for several strengths of interlayer pair tunneling and $\Omega_D = 20meV$	64

4.20	The magnetic neutron scattering intensity at $T = 0K$ for several strengths of interlayer pair tunneling and an increased in-plane cutoff of $\Omega_D = 200meV$.	66
4.21	$1/\lambda^2(T)$ calculated in the strong coupling limit using the tetrahedron method.	69
4.22	$1/\lambda^2(T)$ calculated in the strong coupling limit using direct \mathbf{k} summation.	70
4.23	The structure of the gap at the first Matsubara frequency. Here, $T_J = 40meV$ and $T = 40K$.	72
4.24	The structure of the gap at the first Matsubara frequency. Here, $T_J = 40meV$ and $T = 90K$.	73
4.25	The structure of the gap at the first Matsubara frequency. Here, $T_J = 0meV$ and $T = 40K$.	74
4.26	The structure of the gap at the first Matsubara frequency. Here, $T_J = 0meV$ and $T = 90K$.	75
4.27	The structure of $Z(\mathbf{k})$ at the first Matsubara frequency. Here, $T_J = 40meV$ and $T = 40K$.	76
4.28	The structure of $Z(\mathbf{k})$ at the first Matsubara frequency. Here, $T_J = 40meV$ and $T = 90K$.	76
4.29	The structure of $\chi(\mathbf{k})$ at the first Matsubara frequency. Here, $T_J = 40meV$ and $T = 40K$.	77
4.30	The structure of $\chi(\mathbf{k})$ at the first Matsubara frequency. Here, $T_J = 40meV$ and $T = 90K$.	77

Acknowledgement

There are many people to whom I owe thanks for helping me throughout the course of my career here at Brock University. I would like to begin by thanking all of the professors with whom I have had the opportunity to take classes. Dr. Mitrović, Dr. Black, Dr. Bose, Dr. Reedyk, Dr. Sternin, Dr. Shukla, and Dr. Razavi, you all show an incredible amount of dedication and your passion for physics is inspiring.

Next, I would like to acknowledge my family and express my thanks for their patience with me while living at home and completing this work. Your love and support is always appreciated.

Also to Buddy, thanks for always greeting me with a kiss and being happy to see me. You've grown up so fast I can hardly believe it! But you'll always be my special puppy.

I want to extend a special thanks to all of the good friends with whom I have had the opportunity to share many years at Brock. In particular, I want to acknowledge Mylo and Sarkis, my favourite classmates. Can you believe it - no more assignments?! Myles, thanks for making the rest of us look bad with your unbelievable dedication and hard work! Do you never sleep? Congratulations on a job well done, you deserve it. You still owe me a movie. Mr. Tarkis, you've always made me see the humour in any situation and can bring me to tears with laughter. We've made it through many courses together, and we both know we carried Mylo in 5P41!!

To Anne, thank you for always lighting up my mailbox, I always look forward to your hilarious emails! You've been a great friend. I only wish we had got to know each other sooner, but I know we still have lots of laughs to come in the future. You will always be the undisputed ROTW.

Ron, I thank you for the many conversations and trips to the store that we've shared together. And of course, I can't forget to thank you for the unlimited use of your phone, as well as for answering my MANY computer related questions! Best of luck in where your future leads you.

To Gord, thanks for the many laughs we've shared together. We've always got the memories of the Wolfman and Squinty, among many, many others. I'll see you when we're 70.

I would also like to thank Rodica for sharing many conversations and lunch breaks with me. Also, thank you to Frank and Alice for their assistance in many ways over the years.

I owe a thanks to our physics baseball team as well. We didn't pull off a championship this year, but we had fun trying. Aaron (Tiger Woods), Wes, Mike, Kevin, Dr. Reedyk, Adan, Emily - best of luck to you all in the future.

Finally, I owe a huge debt of gratitude to my supervisor, Dr. B. Mitrović. You have been incredibly patient with me and were always willing to answer my many questions. Thank you for allowing me to work under your supervision and for having the confidence in my abilities that I sometimes lacked myself.

Chapter 1

INTRODUCTION

The field of high temperature superconductivity has had many exciting moments since the discovery of the first superconductor with a transition temperature greater than $30K$. This event occurred in 1986, and physicists Bednorz and Müller were awarded a Nobel Prize for their work on $\text{La}_{2-x}\text{Ba}_x\text{CuO}_4$ shortly thereafter. Since that time, many new high temperature superconducting materials have been discovered, some with superconducting transition temperatures as high as $130K$. Much of the subsequent work by experimentalists and theoreticians has increased the knowledge and understanding of these materials, and led to the development of new and precise techniques for performing measurements. Yet despite all of the advancements in the field of high temperature superconductivity, there still exists no one theory which can account for all of the experimentally observed properties.

This work investigates one particular model which was proposed by Chakravarty, Sudbø, Anderson, and Strong [1] in 1993. They suggest that their Interlayer Pair Tunneling (ILPT) model may provide the mechanism responsible for producing such high transition temperatures in these new materials. Their calculations of the Knight shift and the neutron scattering intensity [3, 4] using the ILPT model have shown results in agreement with experiments. Further support for the model was also found in a recent work by Mitrović and Castle [2] which involved refining the ILPT model to include the strong coupling effects resulting from in-plane interactions. In this case it was found that within this strong coupling formalism there was good agreement with experiments for

calculations of both the isotope effect and the dependence of the critical temperature on in-plane impurities.

The main goal of the present research is to determine whether the ILPT model can describe the dependence of the in-plane magnetic field penetration depth on temperature. The penetration depth is an important property of a superconductor and it can reveal clues about the symmetry of the order parameter. Clearly then, the question of whether or not the ILPT model can reproduce the results of penetration depth experiments is an important one when considering the validity of the model.

The focus in this research is on the high temperature superconductor $\text{YBa}_2\text{Cu}_3\text{O}_{7-x}$ (YBCO). This compound is widely studied because of its relatively simple structure and the high degree of quality to which YBCO samples are made. Understanding the structure of high temperature superconductors (HTSC) is essential for interpreting experiments and developing new theories to try to explain the behaviour of these materials. In the following sections, the structure of YBCO is described briefly, and previous penetration depth experiments conducted on YBCO samples are summarized.

1.1 Structure of YBCO

The new class of HTSC's are layered compounds which are variations on the perovskite crystal having the chemical formula ABO_3 . Typically, these materials have more than one A atom, which is true in the case of YBCO.

A unit cell of YBCO is shown in Figure 1.1 and the layered structure is clearly evident. The unit cell consists of two CuO_2 planes, separated by an yttrium atom, two BaO planes, and finally copper oxide chains at the top and bottom of the cell. The CuO_2 planes are widely thought to be the most important structural element of the material and the location in which superconductivity takes place. The "missing" oxygens in the

CuO chains cause the cell to be slightly orthorhombic ($a \neq b$). When $\text{YBa}_2\text{Cu}_3\text{O}_{7-x}$ is doped such that further oxygen vacancies appear in the chains (i.e. $x \geq 0$), the lattice parameters a and b are slightly distorted. The optimal doping for YBCO is at $x \approx 0.05$, and the critical temperature is 93K . For $x = 0.5$, the vacancy can occur along either the a or b direction with equal probability and the crystal adopts a tetragonal symmetry ($a = b$). For $x \geq 0.5$, there is no superconductivity in $\text{YBa}_2\text{Cu}_3\text{O}_{7-x}$. Typical unit cell dimensions for YBCO are $a = 3.8227\text{\AA}$, $b = 3.8872\text{\AA}$, and $c = 11.6802\text{\AA}$ [5].

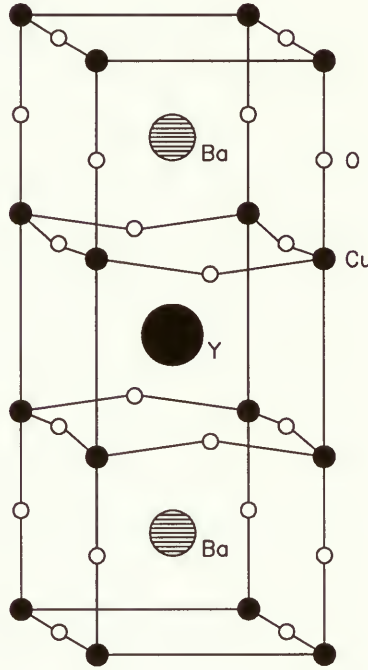


Figure 1.1: $\text{YBa}_2\text{Cu}_3\text{O}_7$ unit cell

1.2 Experimental Penetration Depth Data

Experiments designed to measure the magnetic field penetration depth are difficult to perform accurately. Typically, experimentalists measure the deviation of the penetration

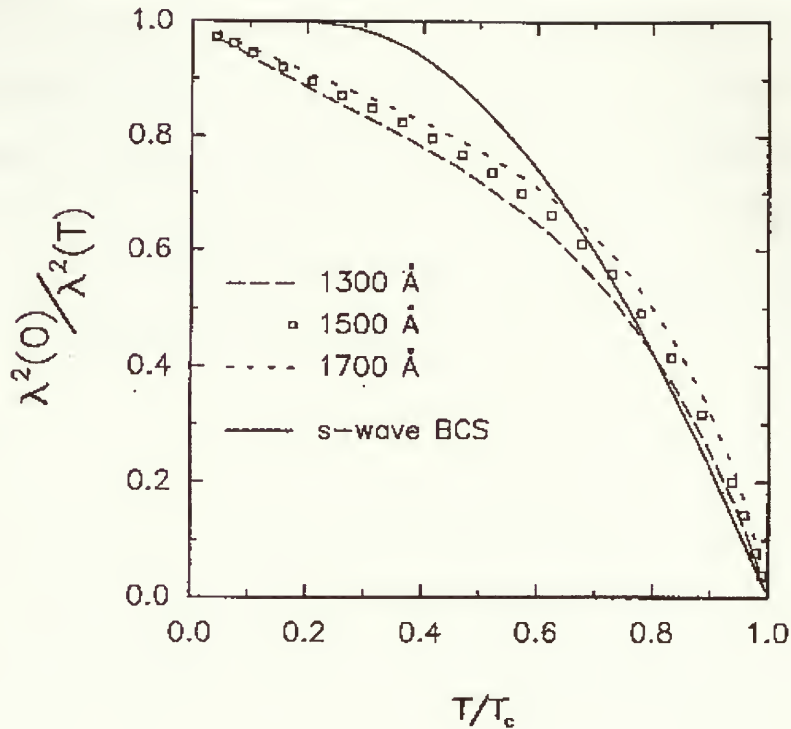


Figure 1.2: Experimental results for the penetration depth in $\text{YBa}_2\text{Cu}_3\text{O}_{6.95}$

depth at a temperature T from its zero temperature value;

$$\Delta\lambda(T) = \lambda(T) - \lambda(0). \quad (1.1)$$

From this data experimentalists can then calculate the quantity $(\lambda(0)/\lambda(T))^2$ which is useful since it is proportional to the normalized superfluid density $n_s(T)/n_0$.

Hardy, Bonn, Morgan, Liang, and Zhang [6] recently presented their results for penetration depth measurements on high quality single crystal samples of $\text{YBa}_2\text{Cu}_3\text{O}_{6.95}$. A plot of their experimental results is shown in Figure 1.2. They also show the traditional s-wave curve obtained within the Bardeen, Cooper, and Schrieffer (BCS) theory

for comparison's sake. Such a well defined linear behaviour at low temperatures had not been observed prior to their work, and their precision microwave measurements provided strong evidence that the gap has $d_{x^2-y^2}$ symmetry. The observed linear temperature dependence of $(\lambda(0)/\lambda(T))^2$ at low temperatures is qualitatively very different from the s-wave BCS result. A constant value of $(\lambda(0)/\lambda(T))^2$ at low temperatures reflects the presence of a gap in the excitation spectrum of a conventional BCS superconductor, while a linear change in $(\lambda(0)/\lambda(T))^2$ with temperature is consistent with d-wave symmetry for which there are nodes in the gap function.

1.3 Overview

The preceding discussion has focused on the rationale for this work, as well as the experimental penetration depth results on YBCO samples. The remainder of the paper moves to the bulk of the present research. The following chapter details the theoretical framework of the ILPT model, as well as the equations for the magnetic field penetration depth. As well, the chapter briefly considers calculations of the magnetic neutron scattering intensity and the Knight shift within the ILPT model. Chapter 3 discusses computational details and addresses some of the numerical difficulties which arise due to the structure of the formulae. The results are presented in Chapter 4 together with a general discussion of the data. Finally, Chapter 5 summarizes the results and presents the conclusions arising from this study of the ILPT model and the magnetic field penetration depth.

Chapter 2

THEORY

This chapter presents the theoretical framework within which the calculations of this research were performed. The Interlayer Pair Tunneling (ILPT) Model is described first, and is then generalized to include the strong coupling effects associated with in-plane interactions. The equations in the BCS limit are also presented, followed by derivations of the magnetic field penetration depth, Knight shift, and magnetic neutron scattering intensity.

2.1 The Interlayer Pair Tunneling Model

The essential feature of the Interlayer Pair Tunneling (ILPT) model of Chakravarty *et al.* [1] is a hopping of electron Cooper pairs between adjacent CuO_2 layers of the unit cell. The hopping of Cooper pairs from layer to layer acts to enhance the amount of pairing that occurs within the individual planes. In the superconducting state, the quasiparticle picture is taken to be approximately valid for motion within a layer, but here the coherent single particle tunneling in the c -direction is prohibited due to strong ab -plane electronic correlation effects. Consequently, single electrons suffer what is known as the “orthogonality catastrophe”, whereas Josephson tunneling of Cooper pairs between adjacent layers is permissible. The ab -plane electron motion for chemical potential μ and lattice constant a is approximated by the tight binding electronic dispersion relation

$$\varepsilon_{\mathbf{k}} = -2t[\cos(k_x a) + \cos(k_y a)] - 4t' \cos(k_x a) \cos(k_y a) - \mu. \quad (2.1)$$

Here, t and t' represent the amount of hopping between the nearest and next nearest neighbour lattice sites, respectively, and the two dimensional wave vector $\mathbf{k} = (k_x, k_y)$ spans the first Brillouin zone. Note that throughout this work the dispersion is calculated relative to the chemical potential μ .

An important feature of the model is that it is independent of the particular in-plane pairing mechanism. The research in this paper considers two scenarios for the in-plane interaction. First, the case of antiferromagnetic spin fluctuation mediated interaction is considered, for which the strong coupling form of the ILPT model is used. Second, the usual BCS weak coupling interaction is applied for both s-wave and $d_{x^2-y^2}$ -wave symmetry of the order parameter.

To describe the coupling of two CuO_2 planes in a unit cell by the interlayer pair tunneling, Chakravarty *et al.* [1] introduce the Josephson pair tunneling term H_J , given as

$$H_J = - \sum_{\mathbf{k}} T_J(\mathbf{k}) [c_{\mathbf{k}\uparrow}^{(1)\dagger} c_{-\mathbf{k}\downarrow}^{(1)\dagger} c_{-\mathbf{k}\downarrow}^{(2)} c_{\mathbf{k}\uparrow}^{(2)} + H.C.] \quad (2.2)$$

where $c_{\mathbf{k}\uparrow}^{(1)\dagger}$ is an electron creation operator for the state having wave vector \mathbf{k} and spin \uparrow in layer (1), and $H.C.$ refers to the Hermitian conjugate. Thus the term $c_{\mathbf{k}\uparrow}^{(1)\dagger} c_{-\mathbf{k}\downarrow}^{(1)\dagger} c_{-\mathbf{k}\downarrow}^{(2)} c_{\mathbf{k}\uparrow}^{(2)}$ can be interpreted to mean the destruction of a pair of electrons with equal and opposite momenta and spin in layer (2) and their subsequent transfer to layer (1), in other words, the tunneling of a Cooper pair from layer (2) to layer (1) with conservation of momentum.

The amount of interlayer hopping is determined by the quantity

$$T_J(\mathbf{k}) = \frac{t_{\perp}^2}{16t} [\cos(k_x a) - \cos(k_y a)]^4, \quad (2.3)$$

where t_{\perp} is a measure of the high-energy single-electron coherent hopping between layers. The form of $T_J(\mathbf{k})$ is based upon the electronic band structure calculations of Andersen *et al.* [7]. Figure 2.1 shows the structure of the function, where a , t , and t_{\perp} have been

set to one for simplicity. Clearly $T_J(\mathbf{k})$ vanishes when $k_x = \pm k_y$, and is maximum when k_x and k_y are such that $(k_x, k_y) = (\pm\pi, 0)$ or $(0, \pm\pi)$.

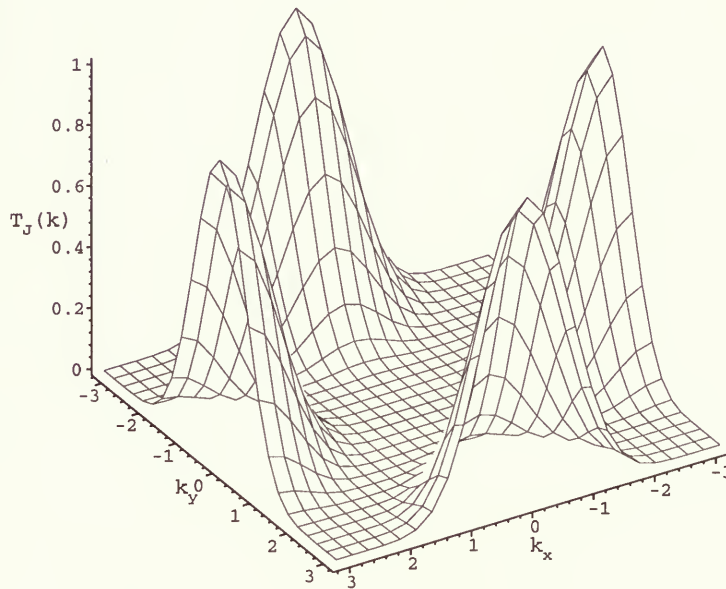


Figure 2.1: The structure of $T_J(\mathbf{k})$.

2.2 Strong Coupling Form of the ILPT Model

The ILPT model of Chakravarty [1] was generalized by Mitrović and Castle [2] to include the strong coupling effects resulting from in-plane interactions. By including these retardation effects it is believed that properties of the superconducting state will exhibit a more accurate dependence on the interaction parameters. Specifically, the dependence of the transition temperature T_c on the interlayer tunneling and in-plane impurities was calculated, as was the oxygen isotope exponent α within the strong coupling formalism [2] with electron-phonon interaction taken for the in-plane pairing mechanism. Results in all cases considered were in good agreement with experiments. There was a dramatic increase in T_c with increasing interlayer pair tunneling and small positive values of α were obtained for high transition temperatures. Furthermore, the critical temperature was strongly suppressed by the presence of in-plane impurity scattering in both the Born and t -matrix approximations. In fact, the convenient manner in which the effects of in-plane disorder can be included in the strong coupling calculations is another advantage of extending the ILPT model to include retardation effects. The T_c dependence on impurities can offer insight into both the order parameter symmetry and pairing mechanism.

According to this strong coupling form of the model, the contribution of the interlayer pair tunneling to the electron self-energy is

$$\hat{\Sigma}_J^{(1)}(\mathbf{k}) = T_J(\mathbf{k})T \sum_m [\phi^{(2)}(\mathbf{k}, i\omega_m)\hat{\tau}_1 + \bar{\phi}^{(2)}(\mathbf{k}, i\omega_m)\hat{\tau}_2]S^{(2)}(\mathbf{k}, m). \quad (2.4)$$

The function $S^{(j)}(\mathbf{k}, m)$ is given by

$$S^{(j)}(\mathbf{k}, m) = \frac{1}{[\omega_m Z^{(j)}(\mathbf{k}, i\omega_m)]^2 + [\varepsilon_{\mathbf{k}}^{(j)} + \chi^{(j)}(\mathbf{k}, i\omega_m)]^2 + |\phi^{(j)}(\mathbf{k}, i\omega_m) + i\bar{\phi}^{(j)}(\mathbf{k}, i\omega_m)|^2} \quad (2.5)$$

Here $Z^{(j)}$ is the renormalization function, $\chi^{(j)}$ is the part of the diagonal self-energy which is even in $i\omega_m$, and $\phi^{(j)}$ and $\bar{\phi}^{(j)}$ are the real and imaginary parts of the pairing

self-energy. T is the temperature expressed in energy units and $\omega_m = \pi T(2m - 1)$ is the m th Matsubara frequency. Note that the self-energy resulting from the interlayer pair tunneling is frequency independent and is purely local in \mathbf{k} , contributing only to the off diagonal pairing self-energy ϕ .

Equation (2.4) was derived assuming the usual form for the total irreducible electron Nambu self-energy in layer (j), namely

$$\hat{\Sigma}^{(j)}(\mathbf{k}, i\omega_n) = i\omega_n(1 - Z^{(j)}(\mathbf{k}, i\omega_n))\hat{\tau}_0 + \phi^{(j)}(\mathbf{k}, i\omega_n)\hat{\tau}_1 + \bar{\phi}^{(j)}(\mathbf{k}, i\omega_n)\hat{\tau}_2 + \chi^{(j)}(\mathbf{k}, i\omega_n)\hat{\tau}_3, \quad (2.6)$$

and with the Dyson equation

$$\hat{G}^{(j)-1}(\mathbf{k}, i\omega_n) = \hat{G}_0^{(j)-1}(\mathbf{k}, i\omega_n) - \hat{\Sigma}^{(j)}(\mathbf{k}, i\omega_n), \quad (2.7)$$

where the non-interacting Green's functions are

$$\hat{G}_0^{(j)}(\mathbf{k}, i\omega_n) = \begin{pmatrix} \frac{1}{i\omega_n - \varepsilon_{\mathbf{k}}^{(j)}} & 0 \\ 0 & \frac{1}{i\omega_n + \varepsilon_{\mathbf{k}}^{(j)}} \end{pmatrix}; \quad j = 1, 2 \quad (2.8)$$

and $\hat{\tau}_0, \hat{\tau}_1, \hat{\tau}_2, \hat{\tau}_3$ are the Pauli matrices.

In order to check that the strong coupling form of the ILPT model reduces to the result of the original model in the BCS limit, one need only consider the weak coupling limit for in-plane interactions and set $Z(\mathbf{k}, i\omega_m) = 1$, $\chi(\mathbf{k}, i\omega_m) = 0$, and $\phi(\mathbf{k}, i\omega_m) = \phi(\mathbf{k})$ accordingly in Equation (2.4). These substitutions reduce the electron self-energy equation to the following form:

$$\hat{\Sigma}_J^{(1)}(\mathbf{k}) = T_J(\mathbf{k})T[\phi^{(2)}(\mathbf{k})\hat{\tau}_1 + \bar{\phi}^{(2)}(\mathbf{k})\hat{\tau}_2] \sum_m \frac{1}{-(i\omega_m)^2 + E_k^2} \quad (2.9)$$

where $E_k^2 = (\varepsilon_{\mathbf{k}}^{(2)})^2 + |\phi^{(2)}(\mathbf{k}) + i\bar{\phi}^{(2)}(\mathbf{k})|^2$. The sum over m in the above equation can be performed using contour integration, using the fact that any function $F(z)$ that is analytic within the contour C_m in the complex z plane may be expressed as

$$F(i\omega_m) = -\frac{\beta}{2\pi i} \oint_{C_m} dz \frac{F(z)}{e^{\beta z} + 1}. \quad (2.10)$$

Then, according to Poisson's summation rule, the sum over m of the function $F(z)$ is

$$\sum_{i\omega_m} F(i\omega_m) = -\frac{\beta}{2\pi i} \oint_C dz \frac{F(z)}{e^{\beta z} + 1}, \quad (2.11)$$

where C is a contour enclosing all of the individual contours C_m . Finally, if $\lim_{|z| \rightarrow \infty} zF(z) = 0$, as is the case here for $F(z) = 1/(-z^2 + E_{\mathbf{k}}^2)$, then the sum reduces to

$$\sum_{i\omega_m} F(i\omega_m) = -2\pi i \times \left[\text{sum of residues of } \frac{F(z)}{e^{\beta z} + 1} \text{ at the poles of } F(z) \right], \quad (2.12)$$

where the residue for a simple pole z_0 of $F(z)$ is found according to the general formula

$$\text{Res}_{(z=z_0)} \frac{p(z)}{q(z)} = \frac{p(z_0)}{q'(z_0)} \quad (2.13)$$

($p(z)$ and $q(z)$ are analytic functions). After using the fact that, in this case, the simple poles of $F(z)$ are $z_0 = \pm E_{\mathbf{k}}$, it can be shown with some algebraic manipulation that Equation (2.9) can be written as

$$\hat{\Sigma}_J^{(1)}(\mathbf{k}) = T_J(\mathbf{k})[\phi^{(2)}(\mathbf{k})\hat{\tau}_1 + \bar{\phi}^{(2)}(\mathbf{k})\hat{\tau}_2] \frac{1}{2E_{\mathbf{k}}} \tanh\left(\frac{E_{\mathbf{k}}}{2T}\right). \quad (2.14)$$

This is the same result as that which was obtained by Chakravarty *et al.* in their original work [1], and the strong coupling formalism does in fact recover the BCS-like form in the weak coupling limit.

Having derived the expression for the electron self-energy due to the interlayer pair tunneling process, Equation (2.4), the contribution to the self-energy arising from the in-plane spin fluctuation interaction can now be considered. The total self-energy $\hat{\Sigma}^{(1)}(\mathbf{k}, i\omega_n)$ is simply a sum of the contributions from these pair tunneling and one boson exchange (i.e. spin fluctuation) processes:

$$\hat{\Sigma}^{(1)}(\mathbf{k}, i\omega_n) = \hat{\Sigma}_{sf}^{(1)}(\mathbf{k}, i\omega_n) + \hat{\Sigma}_J^{(1)}(\mathbf{k}, i\omega_n). \quad (2.15)$$

As in [8], the spin fluctuation contribution can be expressed as

$$\hat{\Sigma}_{sf}^{(1)}(\mathbf{k}, i\omega_n) = T \sum_m \sum_{\mathbf{k}'} P_s(\mathbf{k} - \mathbf{k}', i\omega_n - i\omega_m) \hat{\tau}_0 \hat{G}(\mathbf{k}', i\omega_m) \hat{\tau}_0, \quad (2.16)$$

where $P_s(\mathbf{q}, i\omega_n - i\omega_m)$ is the spin fluctuation propagator defined as

$$P_s(\mathbf{q}, i\omega_n - i\omega_m) = \frac{3}{2}U^2\chi_s(\mathbf{q}, i\omega_n - i\omega_m). \quad (2.17)$$

Here, U is the Hubbard interaction constant and the spin susceptibility $\chi_s(\mathbf{q}, i\omega_n - i\omega_m)$ has the form

$$\chi_s(\mathbf{q}, i\omega_n - i\omega_m) = \chi_\Gamma \int_0^\infty d\Omega P(\Omega) \frac{2\Omega}{(\omega_n - \omega_m)^2 + \Omega^2} \sum_{\mathbf{Q}} \frac{\Gamma}{(q_x - Q_x)^2 + \Gamma^2} \frac{\Gamma}{(q_y - Q_y)^2 + \Gamma^2} \quad (2.18)$$

where $P(\Omega)$ represents the frequency distribution function and χ_Γ is found from the normalization of $P(\Omega)$ to 1. As in the work of Kostur and Mitrović [8], the spectral function $P(\Omega)$ represents the density of spin fluctuation excitations at an energy Ω and is taken to be a continuous distribution of spin fluctuation modes;

$$P(\Omega) = \left[\frac{\Omega}{\omega_0} \Theta(\omega_0 - \Omega) + \frac{1}{\Omega} \Theta(\Omega - \omega_0) \Theta(\omega_{max} - \Omega) \right] / \left[\ln \frac{\omega_{max}}{\omega_0} + \frac{1}{2} \right], \quad (2.19)$$

where $\Theta(\omega_0 - \Omega)$ is the usual step function.

Note that this spin susceptibility contains a key feature of four sharp peaks at the corners of a square Brillouin zone, as represented by the sum over $\mathbf{Q} = (\pm\pi, \pm\pi)$. The presence of these sharp peaks has been well established by magnetic neutron scattering measurements and through calculations of χ_s for a 2D Hubbard model. Kostur and Mitrović [8] exploited this feature of $\chi_s(\mathbf{q}, i\omega_n - i\omega_m)$ by assuming that the peaks are sharp enough so that they may be replaced with a delta function at the four corners of the Brillouin zone, and this assumption will be made in this work as well. This approximation means that the width Γ of the peaks approaches zero. The advantage of making such an approximation is that when considering an integral involving a product of $\chi_s(\mathbf{q}, i\omega_n - i\omega_m)$ and any smooth function of momentum, the only contribution to the integral is from the value of the function at the four corners. With this simplification,

Equation (2.18) reduces to

$$\chi_s(\mathbf{q}, i\omega_n - i\omega_m) = \pi^2 \chi_\Gamma \int_0^\infty d\Omega P(\Omega) \frac{2\Omega}{(\omega_n - \omega_m)^2 + \Omega^2} \sum_{\mathbf{Q}} \delta(\mathbf{q} - \mathbf{Q}), \quad (2.20)$$

and using

$$\lambda_s(n - m) = \frac{3U^2 \chi_\Gamma}{\pi} \int_0^\infty d\Omega P(\Omega) \frac{\Omega}{(\omega_n - \omega_m)^2 + \Omega^2} \quad (2.21)$$

one finds that the electron self-energy can be expressed as

$$\hat{\Sigma}_{sf}(\mathbf{k}, i\omega_n) = \pi T \sum_m \lambda_s(n - m) \frac{1}{4} \sum_{\mathbf{Q}} \hat{\tau}_0 \hat{G}(\mathbf{k} + \mathbf{Q}, i\omega_m) \hat{\tau}_0. \quad (2.22)$$

As in the case of the self-energy due to pair tunneling, the Nambu Green's function $\hat{G}(\mathbf{k}, i\omega_n)$ is found using the non-interacting Green's functions (Equation (2.8)) and the Dyson's equation (Equation (2.7)). After some algebra the form of $\hat{\Sigma}_{sf}(\mathbf{k}, i\omega_n)$ looks like

$$\begin{aligned} \hat{\Sigma}_{sf}(\mathbf{k}, i\omega_n) &= -\pi T \sum_m \lambda_s(n - m) \frac{1}{4} \times \\ &\sum_{\mathbf{Q}} [i\omega_m Z(\mathbf{k} + \mathbf{Q}, i\omega_m) \hat{\tau}_0 + (\varepsilon_{\mathbf{k}+\mathbf{Q}} + \chi(\mathbf{k} + \mathbf{Q}, i\omega_m)) \hat{\tau}_3 + \\ &\phi(\mathbf{k} + \mathbf{Q}, i\omega_m) \hat{\tau}_1 + \bar{\phi}(\mathbf{k} + \mathbf{Q}, i\omega_m) \hat{\tau}_2] S(\mathbf{k} + \mathbf{Q}, m). \end{aligned} \quad (2.23)$$

At this stage, the total self-energy $\hat{\Sigma}^{(j)} = \hat{\Sigma}_J^{(j)} + \hat{\Sigma}_{sf}^{(j)}$ is known and it is possible to extract the equations for Z , χ , and ϕ by equating the two representations for the total self-energy, namely Equations (2.6) and (2.15). These relations are

$$Z(\mathbf{k}, i\omega_n) = 1 + \frac{\pi T}{\omega_n} \sum_m \lambda_s(n - m) \frac{1}{4} \sum_{\mathbf{Q}} [\omega_m Z(\mathbf{k} + \mathbf{Q}, i\omega_m)] S(\mathbf{k} + \mathbf{Q}, m) \quad (2.24)$$

$$\chi(\mathbf{k}, i\omega_n) = -\pi T \sum_m \lambda_s(n - m) \frac{1}{4} \sum_{\mathbf{Q}} [\varepsilon_{\mathbf{k}+\mathbf{Q}} + \chi(\mathbf{k} + \mathbf{Q}, i\omega_m)] S(\mathbf{k} + \mathbf{Q}, m) \quad (2.25)$$

$$\begin{aligned} \phi(\mathbf{k}, i\omega_n) &= -\pi T \sum_m \lambda_s(n - m) \frac{1}{4} \sum_{\mathbf{Q}} \phi(\mathbf{k} + \mathbf{Q}, i\omega_m) S(\mathbf{k} + \mathbf{Q}, m) + \\ &T_J(\mathbf{k}) T \sum_m \phi(\mathbf{k}, i\omega_m) S(\mathbf{k}, m). \end{aligned} \quad (2.26)$$

The equation for $\bar{\phi}$ is identical to the equation for ϕ , and one can choose the phase of the pairing self-energy such that it is purely real, i.e. $\bar{\phi} = 0$. Note that in the above equation

for $\phi(\mathbf{k}, i\omega_n)$ it is assumed that for a given \mathbf{k} and m , the functions $Z(\mathbf{k}, i\omega_n)$, $\chi(\mathbf{k}, i\omega_n)$, and $\phi(\mathbf{k}, i\omega_n)$ are the same in layers (1) and (2).

2.2.1 Equations at the Critical Temperature

To determine the transition temperature T_c , note that the pairing self-energy $\phi(\mathbf{k}, i\omega_n)$ (Equation (2.26)) approaches zero as the temperature T approaches T_c from below. At $T = T_c$, the form of the equation for $\phi(\mathbf{k}, i\omega_n)$ represents an eigenvalue problem, and defining

$$u(\mathbf{k}, n) = \phi(\mathbf{k}, i\omega_n), \quad (2.27)$$

T_c can be found from solving the eigenvalue equation

$$u(\mathbf{k}, n) = \sum_m K(\mathbf{k}, n, m)u(\mathbf{k}, m). \quad (2.28)$$

Here, the kernel $K(\mathbf{k}, n, m)$ is a temperature dependent real symmetric matrix and is equal to the sum of the contributions from the spin fluctuation interaction,

$$K_{sf}(\mathbf{k}, n, m) = -\pi T \lambda_s (n - m) \frac{1}{4} \sum_{\mathbf{Q}} \frac{1}{[\omega_m Z(\mathbf{k} + \mathbf{Q}, i\omega_m)]^2 + [\varepsilon_{\mathbf{k}+\mathbf{Q}} + \chi(\mathbf{k} + \mathbf{Q}, i\omega_m)]^2}, \quad (2.29)$$

and from the interlayer pair tunneling

$$K_J(\mathbf{k}, n, m) = T_J(\mathbf{k}) T \frac{1}{[\omega_m Z(\mathbf{k}, i\omega_m)]^2 + [\varepsilon_{\mathbf{k}} + \chi(\mathbf{k}, i\omega_m)]^2}. \quad (2.30)$$

At T_c , the functions Z , χ , and the chemical potential μ are determined self-consistently by iterating Equations (2.24) and (2.25) (with ϕ set equal to 0 accordingly) together with the equation for the band filling factor,

$$n = 1 - \frac{4T}{N^2} \sum_{\mathbf{k}} \sum_{n=1}^{\infty} (\varepsilon_{\mathbf{k}} + \chi(\mathbf{k}, i\omega_n)) \frac{1}{[\omega_n Z(\mathbf{k}, i\omega_n)]^2 + [\varepsilon_{\mathbf{k}} + \chi(\mathbf{k}, i\omega_n)]^2}, \quad (2.31)$$

which corresponds to the number of electrons of spin up and spin down per unit cell.

By definition, T_c is the highest temperature at which the largest eigenvalue of the matrix $K(\mathbf{k}, n, m)$ is equal to one. At a given temperature T , the largest eigenvalue of K can be determined using the power method described briefly below.

2.2.2 The Power Method

Because K is a Hermitian matrix, the set of all possible eigenvectors $\{|i\rangle\}$ form a complete set, such that

$$\hat{K}|i\rangle = \lambda_i|i\rangle; \quad i = 1, \dots, m. \quad (2.32)$$

The eigenvalues λ_i of \hat{K} are ordered such that $\lambda_1 > \lambda_2 > \dots > \lambda_m$, and thus the eigenvector $|1\rangle$ corresponds to the eigenvalue λ_1 with the largest modulus. Taking an arbitrary vector $|Y\rangle = \beta_1|1\rangle + \beta_2|2\rangle + \dots + \beta_m|m\rangle$ and operating n times with \hat{K} yields

$$\hat{K}^n|Y\rangle = \lambda_1^n\beta_1|1\rangle + \lambda_2^n\beta_2|2\rangle + \dots + \lambda_m^n\beta_m|m\rangle \quad (2.33)$$

$$= \lambda_1^n \left(\beta_1|1\rangle + \beta_2 \left(\frac{\lambda_2}{\lambda_1} \right)^n |2\rangle + \dots + \beta_m \left(\frac{\lambda_m}{\lambda_1} \right)^n |m\rangle \right) \quad (2.34)$$

If n is large enough ($n = 50$ is sufficient in this work), then all but the leading term can be ignored, so that

$$\hat{K}^n|Y\rangle \approx \lambda_1^n\beta_1|1\rangle. \quad (2.35)$$

Operating one final time with \hat{K} and dividing by the norm of the vector $||\hat{K}^n|Y\rangle|| \approx \lambda_1^n\beta_1$

$$\hat{K} \left(\frac{\hat{K}^n|Y\rangle}{||\hat{K}^n|Y\rangle||} \right) \approx \lambda_1|1\rangle, \quad (2.36)$$

and the largest eigenvalue λ_1 is obtained. The convenience of the power method lies in the fact that only the largest eigenvalue λ_1 is obtained, and no time is wasted in computing the many other eigenvalues of the kernel K .

2.3 ILPT Model in the BCS Limit

In addition to the strong-coupling formalism discussed above, the traditional BCS in-plane interaction was also examined in the present research. In this weak coupling picture, $Z(\mathbf{k}, i\omega_n)$ is set equal to 1, $\chi(\mathbf{k}, i\omega_n)$ is set to 0, and the order parameter is frequency independent (i.e. $\phi(\mathbf{k}, i\omega_n) = \phi(\mathbf{k})$). The usual BCS mean field treatment is applied to the total Hamiltonian

$$H = \sum_{\mathbf{k}, \sigma} E_{\mathbf{k}} c_{\mathbf{k}, \sigma}^{\dagger} c_{\mathbf{k}, \sigma} + \sum_{\mathbf{k}, \mathbf{k}'} V_{\mathbf{k}, \mathbf{k}'} c_{\mathbf{k}\uparrow}^{(i)\dagger} c_{-\mathbf{k}\downarrow}^{(i)\dagger} c_{-\mathbf{k}'\downarrow}^{(i)} c_{\mathbf{k}'\uparrow}^{(i)} + H_J \quad (2.37)$$

where $V_{\mathbf{k}, \mathbf{k}'}$ is the in-plane pairing interaction kernel. The first term in (2.37) is the usual kinetic energy term, while the second term describes the scattering of pairs with opposite momenta between states. H_J is defined in Equation (2.2) and represents the momentum conserving pair tunneling between CuO_2 layers. H can be diagonalized by a Bogoliubov transformation, and after lengthy algebra the gap equation at a finite temperature T looks like

$$\phi(\mathbf{k}) = \frac{T_J(\mathbf{k})}{2E_{\mathbf{k}}} \phi(\mathbf{k}) \tanh\left(\frac{E_{\mathbf{k}}}{2T}\right) + \frac{1}{N^2} \sum_{\mathbf{k}'} V_{\mathbf{k}, \mathbf{k}'} \frac{\phi(\mathbf{k}')}{2E_{\mathbf{k}'}} \tanh\left(\frac{E_{\mathbf{k}'}}{2T}\right) \quad (2.38)$$

where $E_{\mathbf{k}} = \sqrt{\phi(\mathbf{k})^2 + \varepsilon_{\mathbf{k}}^2}$ is the quasiparticle energy.

This present work considers two models for the in-plane attractive kernel. The first is an isotropic s-wave interaction, for which $V_{\mathbf{k}, \mathbf{k}'} = V\Theta(\Omega_D - |\varepsilon_{\mathbf{k}}|)\Theta(\Omega_D - |\varepsilon_{\mathbf{k}'}|)$. The step function $\Theta(\Omega_D - |\varepsilon_{\mathbf{k}}|)$ cuts off the in-plane interaction so that $V_{\mathbf{k}, \mathbf{k}'}$ is nonzero only within a shell of width $2\hbar\Omega_D$ centered around the Fermi surface. Both of the terms in the gap equation are strictly positive, and the structure of $V_{\mathbf{k}, \mathbf{k}'}$ is such that for a given temperature the second term is independent of \mathbf{k} (with the exception of the step function Θ) and consequently any anisotropy in the gap is a direct result of the pair tunneling term $T_J(k)$.

The second model assumes that the symmetry of the component of the order parameter resulting from in-plane interactions has $d_{x^2-y^2}$ symmetry, so that the magnitude of this term depends on the direction in momentum space. For this d-wave anisotropic case the interaction is given as $V_{\mathbf{k},\mathbf{k}'} = V g_{\mathbf{k}} g_{\mathbf{k}'}$, where $g_{\mathbf{k}} = \frac{1}{2}[\cos(k_x a) - \cos(k_y a)]\Theta(\Omega_D - |\varepsilon_{\mathbf{k}}|)$. Clearly both $g_{\mathbf{k}}$ and $T_J(k)$ vanish along the lines $k_x = \pm k_y$, so that the gap is exactly zero here.

As in the strong coupling case, the critical temperature is found by solving an eigenvalue problem at T_c using the power method described earlier. At T_c , the eigenvalue problem looks like

$$v(\mathbf{k}) = \sum_{\mathbf{k}'} K(\mathbf{k}, \mathbf{k}') v(\mathbf{k}'). \quad (2.39)$$

K is a real symmetric matrix equal to the sum of the contributions from the weak coupling in-plane interaction,

$$K_{BCS}(\mathbf{k}, \mathbf{k}') = \frac{1}{N^2} V_{\mathbf{k},\mathbf{k}'} \frac{1}{2E_{\mathbf{k}'}} \tanh\left(\frac{E_{\mathbf{k}'}}{2T}\right), \quad (2.40)$$

and from the interlayer Josephson pair tunneling,

$$K_J(\mathbf{k}, \mathbf{k}') = \delta_{\mathbf{k},\mathbf{k}'} \frac{T_J(\mathbf{k}')}{2E_{\mathbf{k}'}} \tanh\left(\frac{E_{\mathbf{k}'}}{2T}\right), \quad (2.41)$$

where here $E_{\mathbf{k}} = \sqrt{\varepsilon_{\mathbf{k}}^2}$, since $\phi(\mathbf{k}) = 0$ at $T = T_c$.

2.4 The Magnetic Field Penetration Depth

One of the defining properties of a superconducting material is that it expels all magnetic field from its interior so that the magnetic flux density \mathbf{B} is always zero inside the material. Screening currents flow on the surface of the superconductor which in turn generate a magnetic field equal and opposite to the applied field, expelling the field from the bulk of the material. However, these surface currents cannot reside solely on the surface of the

material, since this would imply that the current density would be infinite - a physically impossible scenario. Instead, there is a shallow surface region in which the diamagnetic currents flow, and it is within this region that the opposing magnetic field is generated to cancel out the applied field. It will be shown below that the applied field decays exponentially in this surface layer, and the *London magnetic field penetration depth* is on the order of the thickness of this layer.

To see how the magnetic field decays within the superconductor, one can examine Maxwell's equations in the static limit, so that $\frac{\partial}{\partial t}(\dots) = 0$. Taking the curl of both sides of

$$\nabla \times \mathbf{B} = \frac{4\pi}{c} \mathbf{J} \quad (2.42)$$

and using the relation

$$\mathbf{J} = -\frac{c}{4\pi} \frac{1}{\lambda_L^2(0)} \nabla^2 \mathbf{A} \quad (2.43)$$

for the total current density \mathbf{J} , derived assuming the applied magnetic field is described by the vector potential $\mathbf{A}(\mathbf{r}, t)$ within the traditional BCS formalism, the expression in Equation (2.42) reduces to the differential equation

$$\nabla^2 \mathbf{B} = \frac{1}{\lambda_L^2(0)} \mathbf{B}. \quad (2.44)$$

Here, $\lambda_L(0)$ is the value of the London magnetic field penetration depth at zero temperature, and c is the speed of light. The solution of this equation is

$$B_x(z) = B_x(0)e^{-z/\lambda_L(0)} \quad (2.45)$$

such that the field applied parallel to the surface of a superconductor decays exponentially within the material, as shown in Figure 2.2 (adapted from [9]). The flux density at a distance λ_L inside the material would therefore be $1/e$ of its value at the surface.

Another way to view the penetration depth is as the distance λ_L into the superconducting material which would result in the same amount of flux density inside if the

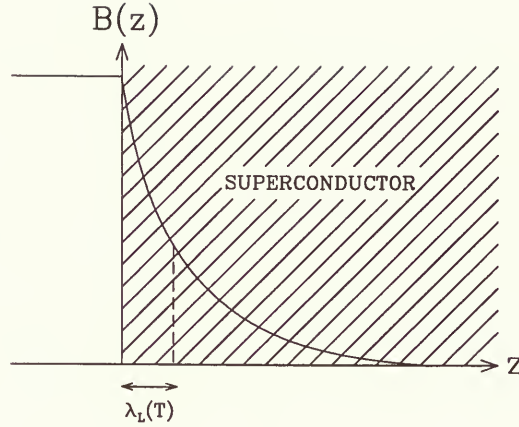


Figure 2.2: The magnetic field penetration depth $\lambda_L(T)$.

external field remained at the constant value of $B(0)$ over this distance. In mathematical terminology,

$$\int_0^\infty dz B_x(z) = \lambda_L B_x(0). \quad (2.46)$$

2.4.1 Strong Coupling Limit

The derivation of the expression for the penetration depth in the strong coupling limit involves lengthy and complicated algebra. This section outlines only the main steps in the procedure and refers the interested reader to any thorough text on many-body theory (see for example, [10]).

To determine the electromagnetic response of a superconductor to an externally applied magnetic field, consider the polarization propagator

$$\Pi^p = \frac{k_B T}{(Na)^2 c} \sum_{\mathbf{k}, i\omega_n} \text{Tr}(ev_x(\mathbf{k}))^2 [\hat{G}(\mathbf{k}, i\omega_n)]^2. \quad (2.47)$$

Here, $v_x(\mathbf{k})$ is the x -component of the Fermi velocity,

$$v_x(\mathbf{k}) = 2ta \sin(k_x a) + 4t' a \sin(k_x a) \cos(k_y a) \quad (2.48)$$

and $\text{Tr}(\dots)$ signifies the trace. In the strong coupling limit, the Green's function is given as

$$\hat{G}(\mathbf{k}, i\omega_n) = \frac{i\omega_n Z(\mathbf{k}, i\omega_n) \hat{\tau}_0 + (\varepsilon_{\mathbf{k}} + \chi(\mathbf{k}, i\omega_n)) \hat{\tau}_3 + \phi(\mathbf{k}, i\omega_n) \hat{\tau}_1}{(i\omega_n Z(\mathbf{k}, i\omega_n))^2 - (\varepsilon_{\mathbf{k}} + \chi(\mathbf{k}, i\omega_n))^2 - \phi^2(\mathbf{k}, i\omega_n)}. \quad (2.49)$$

This is the same Nambu Green's function which was mentioned earlier in the derivation of the self-energy arising from spin fluctuations, and it is found by combining Equations (2.7) and (2.8). To simplify the calculation of the square of the Green's function, note that only the terms proportional to $\hat{\tau}_0$ will survive under the trace operation.

After performing this operation, Equation (2.47) looks like

$$\Pi^p = 2e^2 \frac{k_B T}{(Na)^2 c} \sum_{\mathbf{k}, i\omega_n} (v_x(\mathbf{k}))^2 \frac{-(\omega_n Z(\mathbf{k}, i\omega_n))^2 + (\varepsilon_{\mathbf{k}} + \chi(\mathbf{k}, i\omega_n))^2 + \phi^2(\mathbf{k}, i\omega_n)}{[(\omega_n Z(\mathbf{k}, i\omega_n))^2 + (\varepsilon_{\mathbf{k}} + \chi(\mathbf{k}, i\omega_n))^2 + \phi^2(\mathbf{k}, i\omega_n)]^2}. \quad (2.50)$$

The above expression represents only the paramagnetic contribution to the penetration depth. To determine the contribution arising from the diamagnetic currents, consider the expression in Equation (2.47), but with $\phi(\mathbf{k}, i\omega_n)$ set equal to zero. Performing the same manipulations as above, one finds that

$$\Pi^d = 2e^2 \frac{k_B T}{(Na)^2 c} \sum_{\mathbf{k}, i\omega_n} (v_x(\mathbf{k}))^2 \frac{-(\omega_n Z^N(\mathbf{k}, i\omega_n))^2 + (\varepsilon_{\mathbf{k}} + \chi^N(\mathbf{k}, i\omega_n))^2}{[(\omega_n Z^N(\mathbf{k}, i\omega_n))^2 + (\varepsilon_{\mathbf{k}} + \chi^N(\mathbf{k}, i\omega_n))^2]^2}. \quad (2.51)$$

Note that here the functions $Z^N(\mathbf{k}, i\omega_n)$ and $\chi^N(\mathbf{k}, i\omega_n)$ are the renormalization and diagonal self-energy functions, respectively, evaluated self consistently in the normal state for which $\phi(\mathbf{k}, i\omega_n) = 0$.

In the usual Green's function derivation of the penetration depth [10], the above diamagnetic and paramagnetic contributions are summed and are related to $\lambda(T)$ by

$$\frac{1}{\lambda^2(T)} = \frac{4\pi}{c^2} (\Pi^p - \Pi^d). \quad (2.52)$$

Thus, the expression for the penetration depth in the strong coupling limit is given as

$$\frac{1}{\lambda^2(T)} = \frac{4\pi e^2}{c^2} \frac{2k_B T}{(Na)^2 c} \sum_{\mathbf{k}, n} (v_x(\mathbf{k}))^2 \left\{ \frac{\phi^2(\mathbf{k}, n) + (\varepsilon_{\mathbf{k}} + \chi(\mathbf{k}, n))^2 - (\omega_n Z(\mathbf{k}, n))^2}{[\phi^2(\mathbf{k}, n) + (\varepsilon_{\mathbf{k}} + \chi(\mathbf{k}, n))^2 + (\omega_n Z(\mathbf{k}, n))^2]^2} - \frac{(\varepsilon_{\mathbf{k}} + \chi^N(\mathbf{k}, n))^2 - (\omega_n Z^N(\mathbf{k}, n))^2}{[(\varepsilon_{\mathbf{k}} + \chi^N(\mathbf{k}, n))^2 + (\omega_n Z^N(\mathbf{k}, n))^2]^2} \right\}. \quad (2.53)$$

2.4.2 BCS Limit

In the weak coupling limit, the penetration depth formula is simplified by setting $Z(\mathbf{k}, n) = 1$, $\chi(\mathbf{k}, n) = 0$, and $\phi(\mathbf{k}, n) = \phi(\mathbf{k})$ in the strong coupling result of Equation (2.53). After making these substitutions the relation looks like

$$\frac{1}{\lambda^2(T)} = \frac{4\pi e^2}{c^2} \frac{2k_B T}{(Na)^2 c} \sum_{\mathbf{k}, n} (v_x(\mathbf{k}))^2 \left\{ \frac{\phi^2(\mathbf{k}) + \varepsilon_{\mathbf{k}}^2 - (\omega_n)^2}{[\phi^2(\mathbf{k}) + \varepsilon_{\mathbf{k}}^2 + (\omega_n)^2]^2} - \frac{\varepsilon_{\mathbf{k}}^2 - (\omega_n)^2}{[\varepsilon_{\mathbf{k}}^2 + (\omega_n)^2]^2} \right\}. \quad (2.54)$$

Poisson's summation rule (Equation (2.11)) can be applied to the above sum and the same procedure is followed as was outlined earlier in Equations (2.10) through (2.13).

The general relation

$$\frac{\partial f(y)}{\partial y} = k_B T \sum_n \frac{y^2 - \omega_n^2}{(y^2 + \omega_n^2)^2} \quad (2.55)$$

results from performing the contour integration and is used to derive the equation for the penetration depth in the BCS limit, namely,

$$\frac{1}{\lambda^2(T)} = \frac{4\pi e^2}{c^2} \frac{2}{(Na)^2 c} \sum_{\mathbf{k}} (v_x(\mathbf{k}))^2 \left(\frac{\partial f(E_{\mathbf{k}})}{\partial E_{\mathbf{k}}} - \frac{\partial f(\varepsilon_{\mathbf{k}})}{\partial \varepsilon_{\mathbf{k}}} \right). \quad (2.56)$$

Here, $E_{\mathbf{k}} = \sqrt{\varepsilon_{\mathbf{k}}^2 + \phi^2(\mathbf{k})}$ and $\varepsilon_{\mathbf{k}}$ is the dispersion given in Equation (2.1). The first term in Equation (2.56) depends on temperature through the presence of $\phi(\mathbf{k})$, and results from the paramagnetic part of the current density. Note that the second term, however, is temperature independent and therefore, strictly speaking, it has a constant value. This term results from the diamagnetic part of the current density. It is also important to realize that the term $\frac{\partial f(E_{\mathbf{k}})}{\partial E_{\mathbf{k}}}$ is always negative (or zero) and thus the effect of the paramagnetic contribution is to diminish the diamagnetic contribution.

In the limit of zero temperature, the factor $\frac{\partial f(E_{\mathbf{k}})}{\partial E_{\mathbf{k}}}$ goes to zero and the penetration depth approaches a constant. To determine the value of this constant, consider a special case of spherical symmetry in a free electron model when evaluating the diamagnetic contribution to the current density. Converting the sum over \mathbf{k} to an integral and using

spherical polar coordinates in momentum space, it can be shown that the following relation holds:

$$\frac{1}{(Na)^2 c} \sum_{\mathbf{k}} (v_x(\mathbf{k}))^2 \left(-\frac{\partial f(\varepsilon_{\mathbf{k}})}{\partial \varepsilon_{\mathbf{k}}} \right) = \frac{n}{2m}, \quad (2.57)$$

where n is the electron density and m is the mass of an electron. After making these substitutions into Equation (2.56), the resulting expression is

$$\frac{1}{\lambda_L^2(0)} = \frac{4\pi n e^2}{m c^2}. \quad (2.58)$$

$\lambda_L(0)$ is the London magnetic field penetration depth at zero temperature. Note that this above manipulation is straightforward for this special case of spherical symmetry, but that for the complicated dispersion considered in the present research, it is not trivial to perform this derivation for the diamagnetic contribution $1/\lambda_L^2(0)$. Calculations in the present work do show, however, that this diamagnetic contribution is constant with the form for the tight binding electronic dispersion in Equation (2.1).

The finite temperature penetration depth can also be cast in the same form as the zero temperature result in Equation (2.58). If the superfluid density

$$n_s(T) = \frac{2m}{(Na)^2 c} \sum_{\mathbf{k}} (v_x(\mathbf{k}))^2 \left(\frac{\partial f(E_{\mathbf{k}})}{\partial E_{\mathbf{k}}} - \frac{\partial f(\varepsilon_{\mathbf{k}})}{\partial \varepsilon_{\mathbf{k}}} \right) \quad (2.59)$$

at temperatures above 0K is introduced, then the London penetration depth at a finite temperature T can be expressed as

$$\frac{1}{\lambda_L^2(T)} = \frac{4\pi n_s(T) e^2}{m c^2}. \quad (2.60)$$

2.5 Knight Shift

The Knight shift is a measure of the shift in nuclear magnetic resonance frequency due to the interaction between the nucleus and the electron polarization [10]. Here, only the

shift due to electron spin polarization is considered, and so the Knight shift is really a direct measurement of the electronic spin susceptibility $\chi(0, 0)$.

The procedure for deriving the Knight shift relation in the weak coupling limit is very similar to the derivation of the penetration depth formula. Consider a polarization propagator given as

$$\Pi(0) = -\frac{k_B T \mu_B^2}{(Na)^2 c} \sum_{\mathbf{k}, i\omega_n} \text{Tr}[\hat{G}(\mathbf{k}, i\omega_n)]^2, \quad (2.61)$$

where μ_B is the Bohr magneton, and $\hat{G}(\mathbf{k}, i\omega_n)$ is Equation (2.49) with the weak coupling simplifications $Z(\mathbf{k}, i\omega_n) = 1$, $\chi(\mathbf{k}, i\omega_n) = 0$, and $\phi(\mathbf{k}, i\omega_n) = \phi(\mathbf{k})$, such that

$$\hat{G}(\mathbf{k}, i\omega_n) = -\frac{i\omega_n \hat{\tau}_0 + \varepsilon_{\mathbf{k}} \hat{\tau}_3 + \phi^2(\mathbf{k}) \hat{\tau}_1}{\omega_n^2 + \varepsilon_{\mathbf{k}}^2 + \phi^2(\mathbf{k})}. \quad (2.62)$$

After performing the trace in Equation (2.61), the sum over $i\omega_n$ can be done analytically using Poisson's summation rule, which has already been discussed previously. The resulting spin susceptibility is

$$\chi_0(0, 0) = \Pi(0) = \frac{2\mu_B^2}{(Na)^2 c} \sum_{\mathbf{k}} \left(-\frac{\partial f(E_{\mathbf{k}})}{\partial E_{\mathbf{k}}} \right). \quad (2.63)$$

Finally, to include the repeated scattering between particles and holes, consider the sum of the interactions χ_0 , $\chi_0 U \chi_0$, $\chi_0 U \chi_0 U \chi_0$, ..., such that the total susceptibility is

$$\chi(0, 0) = \chi_0(0, 0)[1 + U\chi_0 + (U\chi_0)^2 + (U\chi_0)^3 + \dots], \quad (2.64)$$

where U is the strength of the Fermi liquid corrections.

Notice that the term in square brackets above is a simple geometric series, and thus the Knight shift can be expressed compactly as

$$K(T) = \chi(0, 0) = \frac{\chi_0(0, 0)}{1 - U\chi_0(0, 0)}, \quad (2.65)$$

with $\chi_0(0, 0)$ given in Equation (2.63).

2.6 Magnetic Neutron Scattering Intensity

In addition to the magnetic field penetration depth and Knight shift calculations, the magnetic neutron scattering intensity in the BCS limit was also calculated in the present research. Following the derivation of Schrieffer [10], one finds that the magnetic neutron scattering intensity is the imaginary part of the spin susceptibility in the superconducting state,

$$\chi(\mathbf{q}, \omega) = \frac{1}{(Na)^2 c} \sum_{\mathbf{k}} \left[A_{\mathbf{k}, \mathbf{q}}^+ \frac{f(E_{\mathbf{k}+\mathbf{q}}) - f(E_{\mathbf{k}})}{\omega - (E_{\mathbf{k}+\mathbf{q}} - E_{\mathbf{k}}) + i\delta} + A_{\mathbf{k}, \mathbf{q}}^- \frac{1 - f(E_{\mathbf{k}+\mathbf{q}}) - f(E_{\mathbf{k}})}{2} \right. \\ \left. \left(\frac{1}{\omega + (E_{\mathbf{k}+\mathbf{q}} + E_{\mathbf{k}}) + i\delta} - \frac{1}{\omega - (E_{\mathbf{k}+\mathbf{q}} + E_{\mathbf{k}}) + i\delta} \right) \right], \quad (2.66)$$

where

$$A_{\mathbf{k}, \mathbf{q}}^{\pm} = \frac{1}{2} \left[1 \pm \frac{(\varepsilon_{\mathbf{k}} - \mu)(\varepsilon_{\mathbf{k}+\mathbf{q}} - \mu) + \phi(\mathbf{k})\phi(\mathbf{k} + \mathbf{q})}{E_{\mathbf{k}} E_{\mathbf{k}+\mathbf{q}}} \right] \quad (2.67)$$

constitute the usual coherence factors and $f(x)$ is the Fermi function. At zero temperature, for which the quantity $\text{Im}\chi(\mathbf{q}, \omega)$ is calculated in the present research, only the term proportional to $A_{\mathbf{k}, \mathbf{q}}^-$ will contribute. Making this simplification, and using the delta representation of a Lorentzian function to condense the equation, the expression for $\text{Im}\chi(\mathbf{q}, \omega)$ looks like [4, 10]

$$\text{Im}\chi(\mathbf{q}, \omega) = \pi \frac{1}{(Na)^2 c} \sum_{\mathbf{k}} \frac{1}{2} \left(1 - \frac{\varepsilon_{\mathbf{k}} \varepsilon_{\mathbf{k}+\mathbf{q}} - \Delta_{\mathbf{k}} \Delta_{\mathbf{k}+\mathbf{q}}}{E_{\mathbf{k}} E_{\mathbf{k}+\mathbf{q}}} \right) \delta(E_{\mathbf{k}} + E_{\mathbf{k}+\mathbf{q}} - \omega). \quad (2.68)$$

The scattering intensity is calculated at the wave vector $\mathbf{Q} = (\pi/a, \pi/a, \pi/c_b)$, where a is the lattice spacing and c_b is the distance between the two CuO layers in a unit cell.

Chapter 3

COMPUTING PROCEDURE

In this chapter, the procedure for calculating the magnetic field penetration depth is outlined in detail for both the strong and weak coupling limits. The computational details are discussed extensively, including the approach to performing the calculations in both momentum and frequency spaces, as well as the difficulties encountered during the computational work due to the structure of the formulae presented in Chapter 2.

3.1 Summations in Momentum and Frequency Space

All of the calculations in this work were performed in momentum space where $\mathbf{k} = (k_x, k_y)$ spans the first Brillouin zone (FBZ) with zone boundaries $k_x = \pm\pi/a$, $k_y = \pm\pi/a$. The FBZ is divided into an $N \times N$ lattice whose size is given as input to the program. Often in computational work, the size of the lattice can have a dramatic effect on the numerical results. It is important to have a large enough lattice size to ensure that the bulk properties of the superconductor will be accurately reflected in the calculations. Lattice sizes of 16×16 and 32×32 are too small for the calculations in this work, because there are not enough \mathbf{k} points over which the momentum dependent quantities are summed to yield reliable results. Theorists typically use at least a 64×64 lattice in numerical calculations but this size was still found to be insufficient to yield a satisfactory degree of accuracy in the present research. For calculations in the BCS limit, a minimum lattice size of 256×256 was used, which the results suggest is large enough to yield values that are trustworthy. A 64×64 lattice in \mathbf{k} space was used for the strong coupling limit, and

it is believed that the small size presents many problems in the results in this limit, as will be discussed in Chapter 4.

There is always an upper limit on the lattice size due to both the memory restrictions of the computing system and to the run time of the programs. The total number of \mathbf{k} points for an $N \times N$ lattice is N^2 , and clearly the memory requirements of the system will increase rapidly as the lattice size grows. Because larger lattices correspond to an increased number of \mathbf{k} points over which the quantities are summed, the total run time of a program can also be unrealistically long and impractical.

Consider for example the strong coupling calculations outlined in Chapter 2, where the calculations involve not only sums over momenta \mathbf{k} , but also sums over Matsubara frequencies. Strictly speaking, the sums over n run from $-\infty \rightarrow \infty$. However, it is not possible numerically to perform a sum over all values of n , and thus the sum is truncated and runs from $-N_c + 1 \rightarrow N_c$, where $N_c = [\omega_c/(2\pi T) + 0.5]$. In these high- T_c materials, the excitations extend to high energies and therefore an energy cutoff of ω_c on the order of a few times the bandwidth is essential in order to realistically represent the materials on a microscopic level. At the same time, N_c is directly proportional to ω_c , and thus a substantial energy cutoff corresponds to a very large value of N_c . This can present enormous size problems, especially at low temperatures, since N_c is also proportional to T^{-1} . There is a delicate balance between choosing a large enough lattice size and cutoff energy ω_c to produce reliable results, and keeping the run time and memory requirements of the program within a reasonable realm.

Fortunately, it is possible to maximize the symmetry of the FBZ region in order to reduce the size and run time of the computer programs. The sums over \mathbf{k} can be transformed to run over the irreducible wedge (IW) only, rather than span the entire FBZ. To illustrate how this is accomplished, consider the symmetry of the FBZ, as shown in Figure 3.1. Any \mathbf{k} point in the FBZ can be reflected or rotated back to the IW

using the C_{4v} point group symmetry of a square lattice, such that

$$\sum_{\mathbf{k} \in \text{FBZ}} f(\mathbf{k}) = \sum_{\mathbf{k} \in \text{IW}} \sum_{R \in C_{4v}} f(R\mathbf{k}) \quad (3.1)$$

is true for an arbitrary function $f(\mathbf{k})$. More specifically, sums over the dispersion $\varepsilon_{\mathbf{k}}$ can be performed over the IW and the results multiplied by a factor of 8. For the lattice sizes considered in this work (typically 64×64 for strong coupling calculations and 256×256 or larger for BCS calculations), the above simplifications can dramatically reduce the memory requirements and run time of a computer program. Consider for example a 64×64 lattice in the spin fluctuation interaction scenario. The total number of \mathbf{k} points in the FBZ is $N^2 = 4096$, while the number of points in the IW is $(\frac{N}{2} + 1)(\frac{N}{2} + 2)/2 = 561$, a notable difference. The advantage of this reduction becomes even more apparent when noting that for each \mathbf{k} point considered, the strong coupling calculations must be

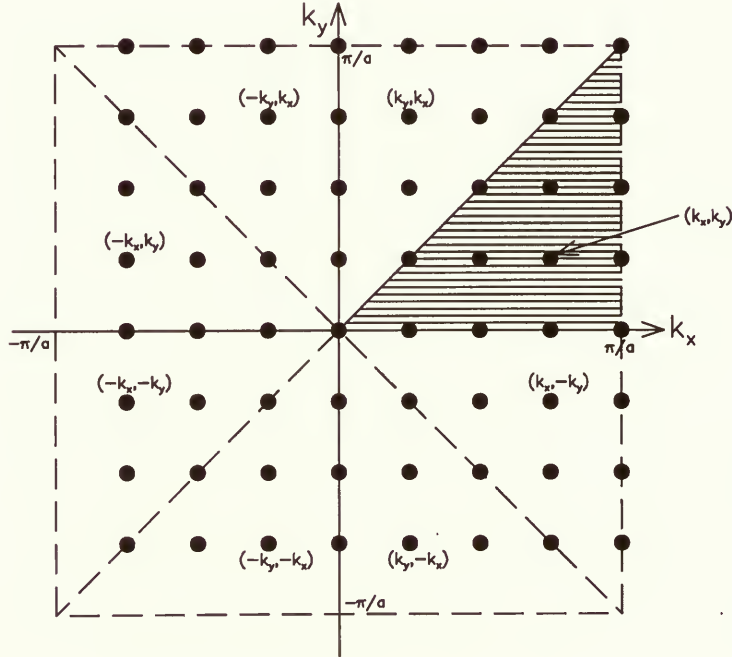


Figure 3.1: The symmetry of the FBZ and the IW (shaded region).

performed for N_c Matsubara frequencies, where N_c can be as high as 300. All of the sums over momenta in both the BCS and strong coupling limits are performed over the irreducible wedge according to the relation in Equation (3.1).

Another means that can be used to reduce the size and run time of the strong coupling programs is to manipulate slightly the sums over Matsubara frequencies such that they run only over positive values of n . As mentioned earlier, the sums over n run from $-\infty \rightarrow \infty$, but they must be truncated due to numerical restrictions so that $-N_c + 1 \leq n \leq N_c$. It is then possible to convert this sum so that n runs from $1 \rightarrow N_c$ only. In general, the relation

$$\sum_{n=-N_c+1}^{N_c} f(n) = \sum_{n=1}^{N_c} [f(-n+1) + f(n)] \quad (3.2)$$

is true for any function of n . Furthermore, the structures of the renormalization function $Z(\mathbf{k}, i\omega_n)$, the diagonal self-energy $\chi(\mathbf{k}, i\omega_n)$, and the pairing self-energy $\phi(\mathbf{k}, i\omega_n)$ are such that these functions are even in $i\omega_n$:

$$\begin{aligned} Z(\mathbf{k}, -i\omega_n) &= Z(\mathbf{k}, i\omega_n) \\ \chi(\mathbf{k}, -i\omega_n) &= \chi(\mathbf{k}, i\omega_n) \\ \phi(\mathbf{k}, -i\omega_n) &= \phi(\mathbf{k}, i\omega_n). \end{aligned} \quad (3.3)$$

This property is important when considering that $\omega_{-n+1} = \pi T(2(-n+1) - 1) = -\omega_n$, so that $Z(\mathbf{k}, i\omega_{-n+1}) = Z(\mathbf{k}, -i\omega_n) = Z(\mathbf{k}, i\omega_n)$ (the same relation holds for χ and ϕ as well) and the sums over n of functions involving Z , χ , and ϕ can be performed from $1 \rightarrow N_c$ and the results multiplied by a factor of 2.

3.2 Strong Coupling Calculations

The first step in approaching the problem of calculating the penetration depth within the strong coupling formalism is to calculate the superconducting transition temperature T_c .

To perform this calculation, standard iterative techniques are used to determine T_c and the band filling factor n , and the quantities Z , χ , and μ are determined self consistently as part of the process. Each iterative loop calculates new, more accurate values for Z , χ , and μ , which are then used to calculate n . The value of n is fixed and is input to the program, and the iterative procedure is carried out until the calculated band filling factor is converged to within a desired accuracy. At this stage the converged values of Z , χ , and μ are used to generate the large kernel $K(\mathbf{k}, n, m)$, whose eigenvalue problem is then solved according to the power method outlined in Chapter 2. T_c is defined as the temperature at which the largest eigenvalue of the matrix K is equal to 1, and a linear interpolation method is used to solve for a more accurate temperature. The entire iterative process is repeated as many times as is necessary to converge the temperature to a sufficient accuracy. This converged temperature is the value of T_c .

Once the value of T_c is obtained, the strong coupling equations are extended to temperatures below T_c . The superconducting gap is finite below T_c , and thus the full forms of Equations (2.24), (2.25) and (2.26) are used with a non-zero ϕ component. An iterative procedure similar to the one used in determining T_c is employed here, and Z , χ , ϕ , and μ are again converged self consistently. Once these solutions are found for both the normal and superconducting states at a temperature $T < T_c$, they can be used to calculate any number of thermodynamic properties. In the present work, the strong coupling solutions are used to calculate the magnetic field penetration depth according to Equation (2.53).

It is instructive at this point to address the issue of performing the sum over $\mathbf{Q} = (\pm\pi, \pm\pi)$ in Equations (2.24), (2.25) and (2.26). Because the calculations are performed over the IW rather than the entire FBZ, it is necessary to reduce the sum over \mathbf{Q} such that all points lie in the IW. For any given \mathbf{k} point in the IW, the location of $\mathbf{k} + \mathbf{Q}$ will fall outside of the IW, so it is necessary to develop a systematic method for transferring

all $\mathbf{k} + \mathbf{Q}$ points back into the IW. Recall that in \mathbf{k} space a translation of $\pm 2\pi$ does not affect the calculations, so each $\mathbf{k} + \mathbf{Q}$ vector can be translated to the point $\mathbf{k} + (-\pi, -\pi)$. Then, according to Figure 3.1, this point can be reflected back into the irreducible wedge using the C_{4v} symmetry transformation $(k_x, k_y) \rightarrow (-k_y, -k_x)$. If this new reflected point is labelled, say, $\bar{\mathbf{k}}$, then it is clear that the sums over \mathbf{Q} in Equations (2.24), (2.25), and (2.26) can be eliminated by using instead the relation

$$\frac{1}{4} \sum_{\mathbf{Q}=(\pm\pi, \pm\pi)} f(\mathbf{k} + \mathbf{Q}) = f(\bar{\mathbf{k}}). \quad (3.4)$$

This way, all quantities are consistent in that they are all calculated over the IW only, which is advantageous from a computing perspective because of the reasons discussed earlier in this chapter.

3.2.1 Penetration Depth Calculation

Consider the calculation of the penetration depth for the strong coupling case (Equation (2.53)). The formula contains a sum in \mathbf{k} space, where \mathbf{k} spans the FBZ. Once again, it is advantageous from a computing perspective to reduce the \mathbf{k} sum to run over the irreducible wedge only, rather than over the entire FBZ. In this case, however, it is incorrect to simply introduce a factor of 8 when reducing the sum to run over the IW because of the presence of the Fermi velocity $v_x(\mathbf{k}) = \frac{1}{\hbar}(\nabla_{\mathbf{k}}\varepsilon_{\mathbf{k}})_x$. This was illustrated by considering a simple test case using $\varepsilon_{\mathbf{k}} = (\hbar\mathbf{k})^2/2m$ (i.e. spherical symmetry) and the sum $\sum_{\mathbf{k} \in \text{FBZ}} (v_x(\mathbf{k}))^2 \delta(E - \varepsilon_{\mathbf{k}})$. Using the relation $\frac{1}{N^2} \sum_{\mathbf{k} \in \text{FBZ}} f(\mathbf{k}) = \frac{1}{N^2} 8 \sum_{\mathbf{k} \in \text{IW}} f(\mathbf{k})$ that was discussed earlier in this chapter, it was found that the plot of $(v_x(\mathbf{k}))^2$ versus $\varepsilon_{\mathbf{k}}$ did not have a slope of $1/2\pi$ as it should. The difficulty arises from the function $(v_x(\mathbf{k}))^2 = \left(\frac{\hbar k_x}{m}\right)^2$, which alone is not invariant under the C_{4v} point group symmetry. This problem was corrected by introducing the symmetric form $[(v_x(\mathbf{k}))^2 + (v_y(\mathbf{k}))^2]/2$

instead of $(v_x(\mathbf{k}))^2$, so that

$$\sum_{\mathbf{k} \in FBZ} (v_x(\mathbf{k}))^2 f(\mathbf{k}) = 8 \sum_{\mathbf{k} \in IW} \frac{(v_x(\mathbf{k}))^2 + (v_y(\mathbf{k}))^2}{2} f(\mathbf{k}). \quad (3.5)$$

The computation of the penetration depth given in Equation (2.53) was performed in two ways. First, the sum over \mathbf{k} was performed directly for a 64×64 lattice, using the solutions found below T_c according to Equations (2.24), (2.25), and (2.26) and the relation in Equation (3.5). In order to verify the calculations and test whether the limited number of \mathbf{k} points significantly affected the results, the penetration depth was also calculated using a different approach entirely. This second method involves converting the sums to integrals over energy and a weighted density of states function. After inserting $\int_{-\infty}^{\infty} dE \delta(E - E_{\mathbf{k}}) = 1$ into both terms of (2.53) and manipulating slightly, the formula looks like

$$\begin{aligned} \frac{1}{\lambda^2(T)} = & \frac{4\pi e^2 2k_B T}{c^2 c} \sum_n \int_{-\infty}^{\infty} dE \frac{1}{(Na)^2} \sum_{\mathbf{k} \in FBZ} (v_x(\mathbf{k}))^2 \times \\ & \left\{ \frac{\phi(\mathbf{k}, n)^2 + (\varepsilon_{\mathbf{k}} + \chi(\mathbf{k}, n))^2 - (\omega_n Z(\mathbf{k}, n))^2}{[\phi(\mathbf{k}, n)^2 + (\varepsilon_{\mathbf{k}} + \chi(\mathbf{k}, n))^2 + (\omega_n Z(\mathbf{k}, n))^2]^2} - \right. \\ & \left. \frac{(\varepsilon_{\mathbf{k}} + \chi^N(\mathbf{k}, n))^2 - (\omega_n Z^N(\mathbf{k}, n))^2}{[(\varepsilon_{\mathbf{k}} + \chi^N(\mathbf{k}, n))^2 + (\omega_n Z^N(\mathbf{k}, n))^2]^2} \right\} \delta(E - E_{\mathbf{k}}), \end{aligned} \quad (3.6)$$

where the superscript N refers to the solutions calculated in the normal state (i.e. when $\phi(\mathbf{k}, n)$ is set equal to zero). The above sum over \mathbf{k} is performed separately for each value of n using the tetrahedron method of Lehmann and Taut [11], which is described next.

3.2.2 The Tetrahedron Method

The general form of the \mathbf{k} sum in Equation (3.6) is

$$A(E) = \frac{1}{\Omega} \sum_{\mathbf{k} \in FBZ} A(\mathbf{k}) \delta(E - E_{\mathbf{k}}) \quad (3.7)$$

where $\Omega = (Na)^2$ is the system volume. Using the fact that $\Delta k_x = \Delta k_y = 2\pi/(Na)$, transforming the sum to an integral, and using a Taylor's series expansion for $E_{\mathbf{k}+\delta\mathbf{k}}$, the

function $A(E)$ can be represented as

$$A(E) = \frac{1}{(2\pi)^2} \int_{E=E_k} \frac{dl}{|\nabla E_k|} A(\mathbf{k}). \quad (3.8)$$

The IW is broken up into $(N/2)^2$ triangles, as illustrated in Figure 3.2, and the contribution of each triangle to the integral above is calculated. To calculate the contribution of a single triangle, consider Figure 3.3 and take $A(\mathbf{k})$ to vary linearly between any 2 points of the triangle. Assuming that $E_1 < E_2 < E_3$, there are four possibilities which may arise. The two simplest cases are when $E \leq E_1$ or $E \geq E_3$, such that the energy contour does not cross through the single triangle being considered. For these two scenarios there is no contribution to $A(E)$.

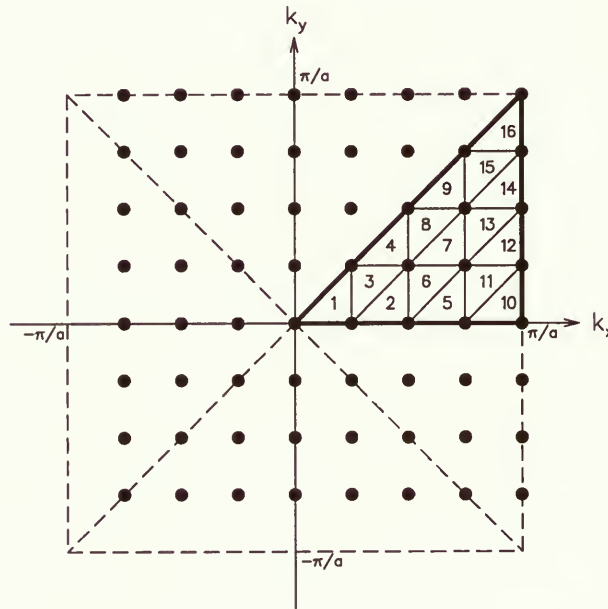


Figure 3.2: The Tetrahedron Method: Division of triangles in the irreducible wedge.

The third possibility is that $E_1 \leq E \leq E_2$, so that the contour crosses the triangle as shown by the line through points 2' and 3' in Figure 3.3. In this instance the integral

has a finite contribution of

$$A_i(E) = \frac{1}{(2\pi)^2} \frac{l(E)}{|\nabla E_{\mathbf{k}}|_{E_{\mathbf{k}}=E}} \bar{A} \quad (3.9)$$

where i labels the triangle being considered and \bar{A} is the value of the function $A(\mathbf{k})$ at the midpoint between $2'$ and $3'$;

$$\begin{aligned} \bar{A} &= \frac{1}{2}(A(2') + A(3')) \\ &= \frac{1}{2} \left[\left(A(1) + \frac{E - E_1}{E_2 - E_1} (A(2) - A(1)) \right) + \left(A(1) + \frac{E - E_1}{E_3 - E_1} (A(3) - A(1)) \right) \right] \end{aligned} \quad (3.10)$$

Next, simple geometry can be used to show that the length of the line segment $l(E)$ is

$$l(E) = 2 \frac{\overline{12'} \overline{13'}}{\overline{12} \overline{13}} \frac{A}{h}; \quad h = \frac{E - E_1}{|\nabla E_{\mathbf{k}}|_{E_{\mathbf{k}}=E}}. \quad (3.11)$$

Here, A is the total area of the single triangle.

Finally, assuming that $E_{\mathbf{k}}$ and $A(\mathbf{k})$ are linear along each side of the triangle such that $\overline{12'} = E - E_1$, $\overline{12} = E_2 - E_1$, etc..., the contribution of triangle i for the case where $E_1 \leq E \leq E_2$ is given as

$$(A_i(E))_{E_1 \leq E \leq E_2} = \frac{1}{(2\pi)^2} 2 \frac{E - E_1}{(E_2 - E_1)(E_3 - E_1)} A \bar{A}, \quad (3.12)$$

with \bar{A} given by Equation (3.10).

The fourth and final possibility is that the energy contour cuts the triangle like the line through the points $2''$ and $3''$ in Figure 3.3. For this case, $E_2 \leq E \leq E_3$, and the same procedure for calculating $A_i(E)$ is followed as in the previous case. The resulting contribution is written as

$$(A_i(E))_{E_2 \leq E \leq E_3} = \frac{1}{(2\pi)^2} 2 \frac{E_3 - E}{(E_3 - E_1)(E_3 - E_2)} A \bar{A}, \quad (3.13)$$

where now the value of $A(\mathbf{k})$ at the midpoint between $2''$ and $3''$ is

$$\bar{A} = \frac{1}{2} \left[\left(A(3) + \frac{E - E_3}{E_2 - E_3} (A(2) - A(3)) \right) + \left(A(1) + \frac{E - E_3}{E_1 - E_3} (A(1) - A(3)) \right) \right]. \quad (3.14)$$

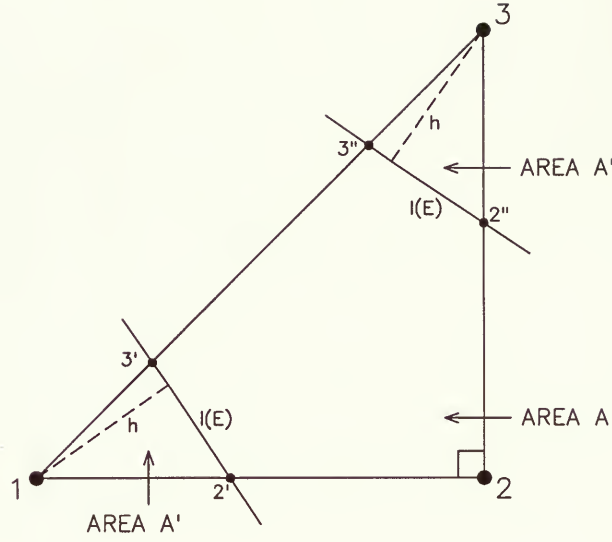


Figure 3.3: The Tetrahedron Method: Energy contour crossing a single triangle i .

The steps performed above are repeated for each triangle shown in Figure 3.2, and the contribution from all $(N/2)^2$ triangles is summed to give $A(E)$ in Equation (3.7). The method can be used repeatedly for each energy value E over which the integral in Equation (3.6) is calculated, and then Simpson's rule of integration is used to perform the integral over energy E . To obtain a value for the penetration depth, the entire procedure must be repeated for each Matsubara frequency. The value obtained after performing the sum over n and multiplying by the necessary prefactors in Equation (3.6) is the value of $1/\lambda^2(T)$ in the strong coupling limit at a temperature T .

This adaptation of the 3D tetrahedron method of Lehmann and Taut to the 2D problem here provides a straightforward and systematic approach to performing the sum in Equation (3.6). The method relies heavily on the assumption that the functions $E_{\mathbf{k}}$ and $A(\mathbf{k})$ vary linearly between any two \mathbf{k} points, which in this case is a reasonable assumption because both functions are smooth and the \mathbf{k} mesh is quite fine. The main motivation for using this method was the limitation of the direct summation over \mathbf{k} points

involving the derivative of the Fermi function $f(E_{\mathbf{k}})$. The term $-\frac{\partial f(E_{\mathbf{k}})}{\partial E_{\mathbf{k}}}$ is sharply peaked near the Fermi line, and so it is possible that the number of \mathbf{k} points is not sufficient to pick up all of the contribution to the penetration depth from this narrow region. Also, the pair tunneling term $T_J(\mathbf{k})$ is purely local in \mathbf{k} and thus one expects the size of the \mathbf{k} mesh to be important in the calculations, especially at low temperatures for which the energy interval $k_B T$ is small. By converting the summation to involve the weighted density of states, there is effectively an interpolation between points based on the values calculated at the discrete \mathbf{k} points, and the function is somewhat “smoothed”.

3.3 BCS Calculations

While the approach to calculating the penetration depth in the weak coupling limit is much the same as for the strong coupling case, the calculations are simplified somewhat because $Z(\mathbf{k}, n) = 1$, $\chi(\mathbf{k}, n) = 0$, and $\phi(\mathbf{k}, n) = \phi(\mathbf{k})$ in this limit. Because there are no sums over Matsubara frequencies in the BCS limit, it is possible to increase the lattice size in momentum space to 256×256 , or in some instances, to 512×512 or even 1024×1024 . The importance of using as large a lattice as possible was discussed earlier in this chapter, and the nature of the BCS calculations allows us to maximize the lattice size while still maintaining programs with a reasonable run time and memory requirement. Nevertheless, there is always some inherent error due to the fact that there is an upper limit on the number of \mathbf{k} points on any computing system. One can never achieve an infinitely fine \mathbf{k} mesh, so it is important to use as large a size as possible.

The critical temperature is calculated using the power method to solve the eigenvalue problem in Equation (2.39), where the kernel $K(\mathbf{k}, \mathbf{k}')$ is the sum of Equations (2.40) and (2.41). Again, the linear interpolation method is used to converge T_c to within a desired accuracy. The gap is found at temperatures below T_c by iterating Equation (2.38) self

consistently for $\phi(\mathbf{k})$.

As in the strong coupling case, the penetration depth in the BCS in-plane interaction is calculated in two ways. The first way is to perform the sum over \mathbf{k} in Equation (2.56) directly, where the momentum vector \mathbf{k} runs only over the IW and the relation in (3.5) is used. The derivative of the Fermi function is calculated using the relation $\frac{\partial f(E_{\mathbf{k}})}{\partial E_{\mathbf{k}}} = [(f(E_{\mathbf{k}}))^2 - f(E_{\mathbf{k}})]/k_B T$ where the Fermi function is $f(E_{\mathbf{k}}) = 1/(e^{E_{\mathbf{k}}/k_B T} + 1)$. The second method makes use of the tetrahedron method which was outlined in detail above, and Simpson's rule of integration is again used to perform the integral over energy E . Without the strong coupling effects included, the tetrahedron method is even easier to work with, since there are no sums over Matsubara frequencies and the function $A(\mathbf{k})$ in Equation (3.7) is much simpler. The formula for the penetration depth to which the tetrahedron method is applied looks like

$$\frac{1}{\lambda^2(T)} = \frac{4\pi e^2}{c^2} \frac{1}{c} \left\{ 2 \int_{-\infty}^{\infty} dE \left(\frac{df(E)}{dE} \right) \frac{1}{(Na)^2} \sum_{\mathbf{k} \in FBZ} (v_x(\mathbf{k}))^2 [\delta(E - E_{\mathbf{k}}) - \delta(E - \varepsilon_{\mathbf{k}})] \right\}. \quad (3.15)$$

In effect, what is being calculated by the tetrahedron method in this BCS limit is a “weighted” density of states. If $A(\mathbf{k}) = 1$, then Equation (3.7) reduces to the relation for the density of states $N(E)$. However, because of the presence of the term $(v_x(\mathbf{k}))^2$ under the summation over \mathbf{k} , the density of states is skewed somewhat from its pure value. These new weighted densities of states, which represent the paramagnetic and diamagnetic portions of the sum in Equation (3.15), respectively, are labelled as

$$N_{v_{\mathbf{k}}}^S(E) = \frac{1}{(Na)^2} \sum_{\mathbf{k} \in FBZ} (v_x(\mathbf{k}))^2 \delta(E - E_{\mathbf{k}}), \quad (3.16)$$

$$N_{v_{\mathbf{k}}}^N(E) = \frac{1}{(Na)^2} \sum_{\mathbf{k} \in FBZ} (v_x(\mathbf{k}))^2 \delta(E - \varepsilon_{\mathbf{k}}). \quad (3.17)$$

After the integration over E and multiplication by the prefactors of (3.15), the value of the inverse of the penetration depth squared with BCS in-plane interaction is obtained.

Chapter 4

NUMERICAL RESULTS AND DISCUSSION

The previous two chapters have examined in detail the theoretical framework of the magnetic field penetration depth, the Knight shift, and the neutron scattering intensity within the ILPT formalism, as well as the computational procedures used in calculating these quantities. This current chapter presents the results of the calculations of this research, accompanied by a general discussion and analysis of the data. The results for the penetration depth, Knight shift, and the neutron scattering intensity in the weak coupling limit are discussed first, followed by the results for the penetration depth in the strong coupling limit.

4.1 BCS Limit

In the BCS in-plane interaction scenario, the input parameters were chosen to comply with the literature values [1] so that meaningful comparisons could be made among the various works. The band parameters are $t = 250meV$ and $t'/t = -0.45$, which are the same values as those in several earlier works [1-4]. The Debye cutoff for in-plane interaction is $\Omega_D = 20meV$, as in [3], although the value of Ω_D is not stated in [4]. The chemical potential $\mu = -315meV$ corresponds to a band filling factor of 0.86 electrons of spin up and down per unit cell, and is also the value taken in [3, 4]. The value of the band filling factor is equal to twice the area under the density of states curve up to the Fermi energy E_F . Figure 4.1 shows a plot of the density of states generated for a 400×400 lattice using the tetrahedron method outlined in Chapter 3. The value of the

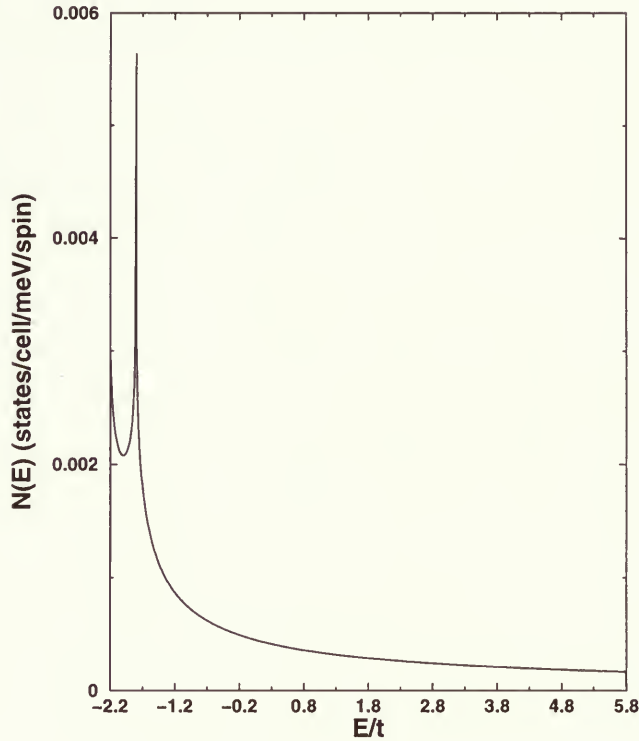


Figure 4.1: Electronic density of states for the tight binding dispersion $\varepsilon_{\mathbf{k}}$.

in-plane pairing interaction V is chosen so as to keep the critical temperature constant and close to the T_c for optimally doped YBCO. The size of the lattice for the momentum space calculations is 256×256 , unless specifically stated otherwise.

4.1.1 Penetration Depth (s-wave Symmetry)

As discussed in Chapter 2, two cases of in-plane interaction were considered in the BCS limit. First, it was the simplest model, which is an isotropic s-wave interaction, that was examined. The penetration depth was calculated using both direct summation over the $N \times N$ lattice in momentum space and the tetrahedron method, as outlined in

Chapter 3. Figure 4.2 shows a plot of $1/\lambda^2(T)$ as a function of reduced temperature T/T_c for several values of interplanar coupling. The values were obtained using the tetrahedron method for a 256×256 lattice. The critical temperature was kept constant at $T_c = 93.66K$ by varying the in-plane pairing interaction V . For interlayer tunneling strengths of $T_J = 0, 10, 20, 30, 40meV$, the value of the in-plane pairing is $V = 999.9, 922.0, 826.4, 699.0, 476.7meV$, respectively. Recalling that T_J is related to the high energy single electron coherent hopping as $T_J = t_\perp^2/t$, it is easily shown that these same strengths of T_J correspond to values of $t_\perp = 0, 35.4, 50.0, 70.7, 86.6, 100.0meV$, respectively.

As T approaches T_c from below, the value of $1/\lambda^2(T)$ approaches zero, as expected, such that the penetration depth is infinite at the critical temperature where the material reverts back to its normal state. As the temperature is decreased from T_c , the size of $1/\lambda^2(T)$ grows until approximately 20% of T_c , at which point the curves level off to a constant value. While all curves shown display these general trends, note that the strength of the interlayer pair tunneling significantly affects the overall shape of the curves. For $T_J = 0$ the curve smoothly turns over to its zero temperature value and is constant at this value below approximately 25% of T_c . The inclusion of pair tunneling results in a “lowering” of the curves and the shape changes from being concave (with respect to the origin) to convex in the mid-temperature range as T_J increases.

The traditional s-wave BCS curve [12] is also included in the plot of Figure 4.2 as a point of reference. It lies close to the $1/\lambda^2(T)$ curves for lower strengths of pair tunneling, such that $0 \leq T_J \leq 20meV$. Note that the usual BCS curve does not fall exactly over the s-wave result calculated with no pair tunneling. The two curves were not expected to coincide because of the differences in the electronic dispersions and Fermi surfaces for the two cases. The original BCS model assumes a spherical Fermi surface and a simple model for the dispersion, where $\varepsilon_k^2 = (\hbar k)^2/2m$, and consequently $v(k) = \hbar k/m$. In

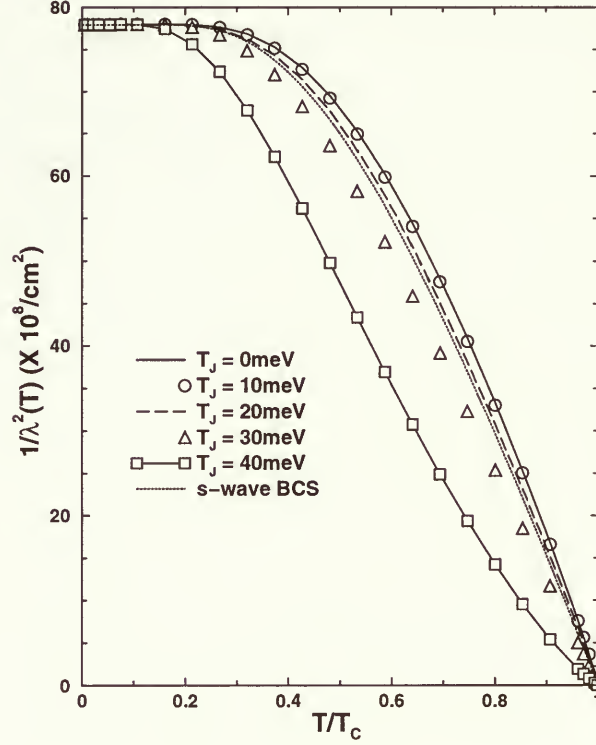


Figure 4.2: The dependence of $1/\lambda^2(T)$ on temperature for several strengths of interlayer tunneling assuming s-wave BCS in-plane interaction.

this study, however, the tight binding dispersion of Equation (2.1) was used, which leads to a non-spherical Fermi surface. Because the penetration depth formula depends on the Fermi velocity $v_x(\mathbf{k}) = \frac{1}{\hbar}(\nabla_{\mathbf{k}}\epsilon_{\mathbf{k}})_x$, one expects the change in dispersion to influence the results. The effect of altering $v_x(\mathbf{k})$ was seen in Chapter 3, where it was stated that this term alone is not invariant under the C_{4v} point group symmetry, and thus a symmetric form was substituted in its place. The results were dramatically different once the change was made. Consequently, it is not surprising to see some difference between the BCS curve and the results calculated with $T_J = 0 \text{ meV}$. Nevertheless, including the

BCS curve gives a point of reference for comparison to the calculated values in this study, and lends support for the accuracy of the results.

It is interesting to examine the disparity between the two methods by which the penetration depth was calculated. Figure 4.3 illustrates how the \mathbf{k} summation method compares to the tetrahedron method for the two extreme values of interplanar coupling, again for a 256×256 lattice. At high temperatures, there is only a slight discrepancy between the two methods, and the \mathbf{k} summation method yields slightly lower values than the tetrahedron method. This difference is less pronounced when the pair tunneling is

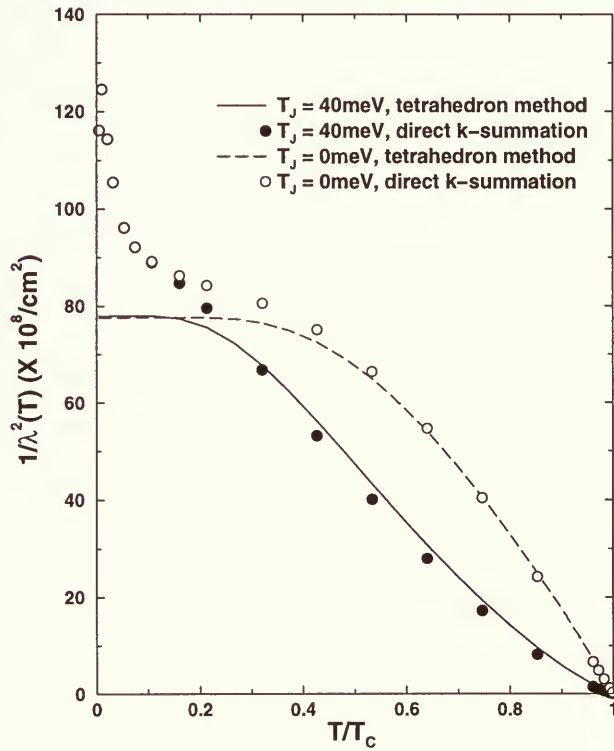


Figure 4.3: Comparison of $1/\lambda^2(T)$ calculated using the tetrahedron method and direct \mathbf{k} space summation assuming s-wave BCS in-plane interaction.

turned off. However, for both $T_J = 0\text{meV}$ and $T_J = 40\text{meV}$ in the \mathbf{k} summation scenario, $1/\lambda^2(T)$ continues to increase as the temperature decreases. When $T_J = 40\text{meV}$, the momentum space calculations start deviating from the tetrahedron method results at about 30% of the critical temperature. For $T_J = 0\text{meV}$, this separation occurs at even higher temperatures, around $T/T_c = 0.4$. It appears that the behaviour of $1/\lambda^2(T)$ at low temperatures in the \mathbf{k} summation method is strictly due to numerics, and does not have any physical significance.

These numerical problems associated with the \mathbf{k} summation method at low temperatures limit the extent to which this approach can be used when calculating the penetration depth. The results from the direct summation below $T/T_c \approx 0.3$ were not trusted, but regardless of the reason for the steep increase in $1/\lambda^2(T)$ at low temperatures, the point of the above comparison between the two methods used is that they both give consistent results in the mid to high temperature range. This is gratifying in that either method can be used with confidence to calculate the penetration depth within this range. Furthermore, the tetrahedron method yields expected results for this s-wave BCS limit at all temperatures, lending support to the validity of this method as a means of calculating the penetration depth.

Examine next the plot of Figure 4.4 showing the structure of the weighted density of states $N_{v_{\mathbf{k}}}^S(E)$ which was generated by the tetrahedron method. The function is plotted for both $T = 1\text{K}$ and $T = 93.5\text{K}$ with an interlayer pair tunneling strength of $T_J = 40\text{meV}$ (recall that $T_c = 93.66\text{K}$ here). The axes labels on the small inset graph are the same as those on the main graph.

The most important structural element to notice in this plot of Figure 4.4 is the gap in energy from 0–6meV for $T = 1\text{K}$. The flattening of the penetration depth curve which was pointed out in Figure 4.2 is directly related to the presence of this gap in the weighted density of states. If $N_{v_{\mathbf{k}}}^S(E)$ is zero then there can be no contribution from the

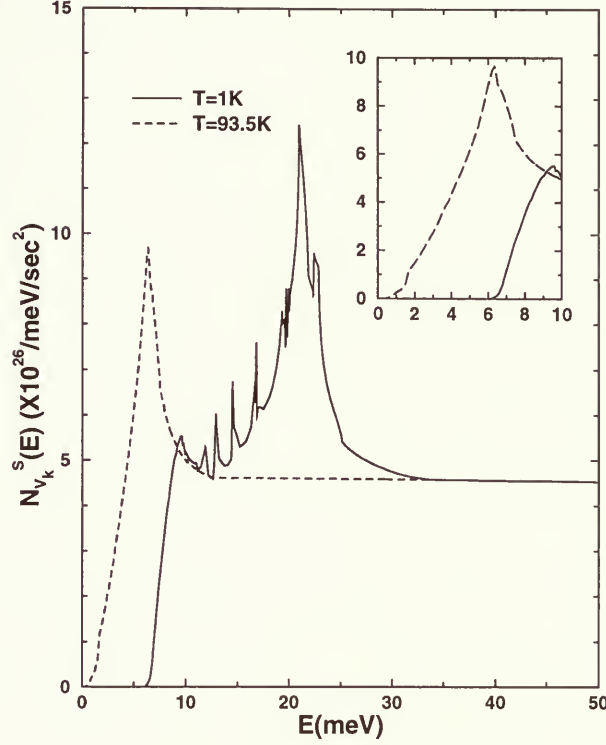


Figure 4.4: The weighted density of states assuming s-wave BCS in-plane interaction with an interlayer tunneling strength of $T_J = 40 \text{ meV}$.

paramagnetic part of the current density (i.e. the term related to $E_{\mathbf{k}} = \sqrt{\varepsilon_{\mathbf{k}}^2 + \phi^2(\mathbf{k})}$) and the penetration depth will result from the constant temperature independent term only. Consequently, at low temperatures for which the gap in the weighted density of states is large, the shape of $1/\lambda^2(T)$ is flat and its value is equal to the value of the term resulting from the diamagnetic part of the current density.

The energy range over which the gap extends is important when considering the structure of the penetration depth relation in the tetrahedron method (Equation (3.15)). The function $N_{v_{\mathbf{k}}}^S(E)$ is multiplied by the derivative of the Fermi function and integrated over

all E . As mentioned in the discussion of the penetration depth in the BCS limit in Chapter 2, the Fermi function derivative tends to zero as the temperature T approaches zero. As the temperature is increased, the size of the gap becomes smaller, and the magnitude of the paramagnetic contribution to $1/\lambda^2(T)$ grows. Note that the contribution from this term is negative and thus the paramagnetic part of the penetration depth diminishes the diamagnetic contribution. At T very close to T_c , the paramagnetic contribution completely cancels the diamagnetic contribution such that $1/\lambda^2(T = T_c) = 0$.

Note also that the two curves in Figure 4.4 each display a sharp peak which is due to the onset of superconductivity, since this feature was not found in the graph of the quantity $N_{v_k}^N(E)$, where $E_k = \varepsilon_k$ in the normal state.

4.1.2 Penetration Depth (d-wave Symmetry)

The second case considered in the BCS limit was the d-wave anisotropic in-plane interaction, where $V_{\mathbf{k},\mathbf{k}'} = V g_{\mathbf{k}} g_{\mathbf{k}'}$ and $g_{\mathbf{k}} = \frac{1}{2}[\cos(k_x a) - \cos(k_y a)]\Theta(\Omega_D - |\varepsilon_{\mathbf{k}}|)$. The results for the penetration depth calculations performed using the tetrahedron method are presented in Figure 4.5, again for five different strengths of pair tunneling. As before, the critical temperature is kept constant by varying the magnitude of V . In this d-wave case, $V = 2458.9, 2136.3, 1779.7, 1364.7, 783.2 meV$ corresponding to pair tunneling strengths of $T_J = 0, 10, 20, 30, 40 meV$, respectively.

As in the s-wave BCS limit, the d-wave curve for $1/\lambda^2(T)$ vanishes at $T = T_c$ as expected, and increases in magnitude as the temperature is decreased from T_c . The behaviour at high temperatures looks much the same as in the s-wave case for all T_J values, except that the slope of the curves is less steep in the d-wave case. The interlayer tunneling again acts to suppress the value of $1/\lambda^2(T)$, and for $T_J = 30 meV$ and $T_J = 40 meV$ the slopes have a convex curvature in the mid-temperature range. Note that this convex curvature is not consistent with the experimental results (see Figure 1.2).

The concave nature of the curves for smaller strengths of pair tunneling is in far better agreement with the experimental curves.

The main structural difference between the s-wave and d-wave BCS limits occurs at low temperatures. Note that the d-wave penetration depth curves do not level off as quickly as the s-wave curves do, and that the d-wave curves are nearly linear in the low temperature region (but above the $0-0.15T/T_c$ range for which the flattening occurs). The flattening of the curves below 15% of T_c is a result of the tetrahedron method itself, and the numbers within this range cannot be considered to be reliable

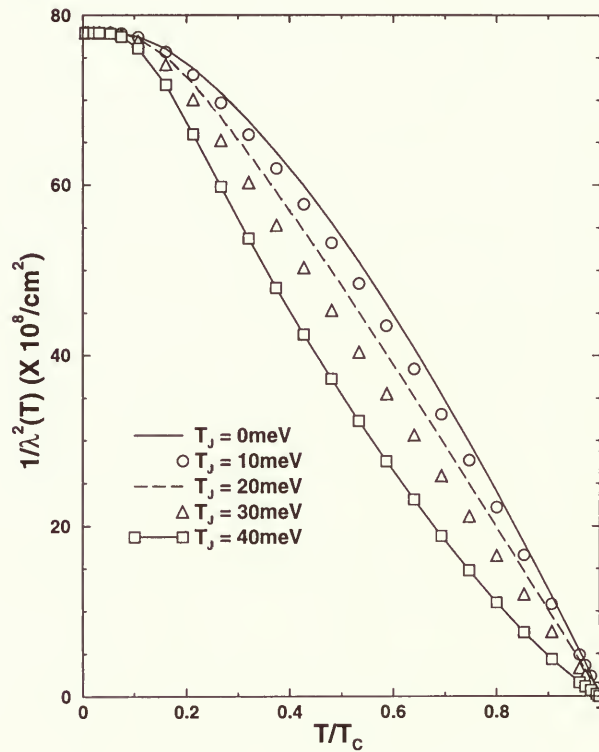


Figure 4.5: The dependence of $1/\lambda^2(T)$ on temperature for several strengths of interlayer tunneling assuming d-wave BCS in-plane interaction.

in this d-wave case. To see why this levelling of $1/\lambda^2(T)$ occurs, examine the plots of $N_{v_k}^S(E)$ shown in Figures 4.6 and 4.7. The weighted density of states is plotted for two temperature values and for the two extreme values of interlayer coupling. For $d_{x^2-y^2}$ symmetry, one expects to find the absence of a gap in the density of states curve. In other words, the density of states should be linear and finite at low energies, and go to zero only at the origin. However, as evidenced by the plots of $N_{v_k}^S(E)$, there is in fact a small gap present in these d-wave calculations for both values of T_J . Following the same reasoning presented in the discussion of the s-wave BCS limit, it is clear that this

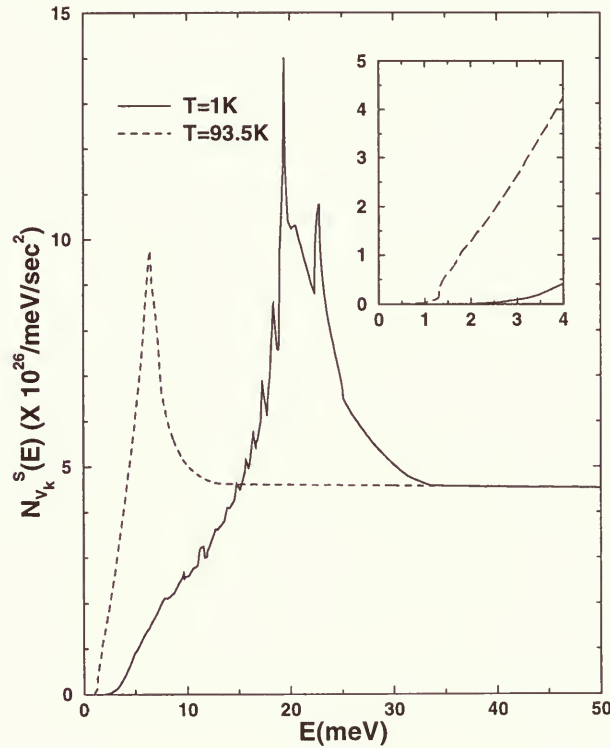


Figure 4.6: The weighted density of states assuming d-wave BCS in-plane interaction with no interlayer pair tunneling.

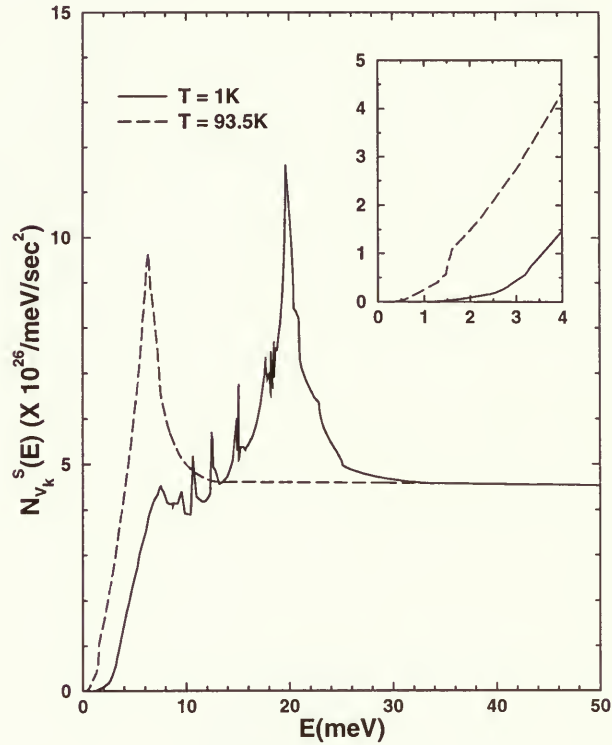


Figure 4.7: The weighted density of states assuming d-wave BCS in-plane interaction with an interlayer tunneling strength of $T_J = 40\text{meV}$.

gap in the d-wave weighted density of states is responsible for the levelling of $1/\lambda^2(T)$ below 15% of T_c . Consequently, the results below this temperature can be disregarded. One can speculate that the penetration depth curves may continue in a linear fashion until $T = 0\text{K}$, which would be consistent with experiments. Note that if one were to extrapolate $1/\lambda^2(T)$ linearly to zero temperature, then $\lambda(0) \approx 1100\text{\AA}$, which is on the correct order of magnitude based on experiments on YBCO [13]. However, one cannot make any definitive statement about the behaviour below $T/T_c = 0.15$; one can only present results as obtained, without extrapolating to zero temperature or attempting to

fit curves to match those of the experiments.

To further explore the notion that numerics are responsible for the levelling off of the penetration depth curve in the d-wave BCS limit, consider the plot showing the structure of $\phi(\mathbf{k})$ in Figure 4.8. The amount of interlayer tunneling here is $T_J = 40\text{meV}$, and the temperature is $0K$. Note the anisotropy of the gap along the Fermi line, which is expected because of the structure of $V_{\mathbf{k},\mathbf{k}'}$ for d-wave symmetry. The gap goes to zero along the lines $k_x = \pm k_y$, and this is consistent with a linear behaviour in the density of states at low energies. Consequently, because this linear behaviour in the (weighted)

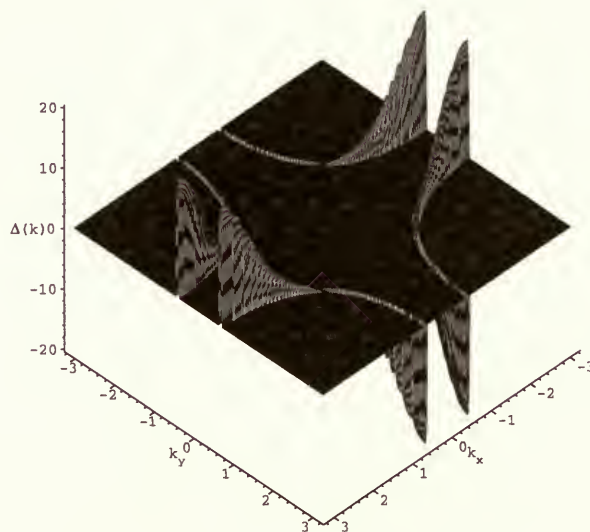


Figure 4.8: The structure of $\phi(\mathbf{k})$ in the BCS limit assuming d-wave symmetry of the in-plane interaction. Here, $T = 0K$ and $T_J = 40\text{meV}$.

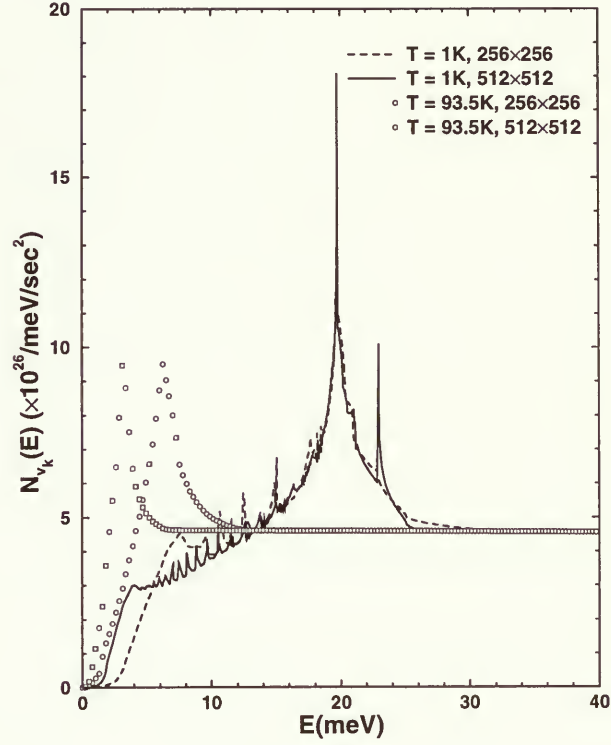


Figure 4.9: The weighted density of states calculated assuming d-wave BCS in-plane interaction for two different lattice sizes with $T_J = 40\text{meV}$.

density of states is not observed, it appears definite that the tetrahedron method itself is responsible for the flattening of $1/\lambda^2(T)$ at low temperatures, and that the calculations of the gap in this research are accurate.

Note also in Figures 4.6 and 4.7 the series of sharp peaks in the energy range of $10\text{--}20\text{meV}$ at a temperature of $T = 1\text{K}$. The peaks are likely due to the numerical method itself and to the limited number of \mathbf{k} points with which the functions $\phi(\mathbf{k})$ and $\varepsilon_{\mathbf{k}}$ are calculated. Figure 4.9 shows a plot of the same function $N_{v_{\mathbf{k}}}^S(E)$ calculated with a 512×512 lattice for $T_J = 40\text{meV}$. The peaks for the larger lattice size are slightly

smaller in size and number, suggesting that the limited size of N is at least partly responsible for their presence. However, these peaks are unimportant in this work and do not influence the results. The reason for this is because they occur at high energies and $N_{v_k}^S(E)$ is multiplied by the Fermi function derivative which is sharply peaked around $E = 0meV$. The width of this peak is on the order of $k_B T$, which is quite narrow for the low temperatures at which the series of peaks are evident. These sharp features occur at much higher energies than the width of this peak. Because the Fermi function derivative is zero over the energy range of the peaks, any contribution from $N_{v_k}^S(E)$ in this vicinity will be cancelled out.

Note also that the size of the d-wave “gap” in the weighted density of states is smaller for a larger lattice. This behaviour confirms the suspicion that the limited number of k points is responsible for the gap in $N_{v_k}^S(E)$ and consequently the flattening of $1/\lambda^2(T)$ in the d-wave case.

To address the issue of the convex curvature for large T_J in the d-wave in-plane interaction case, consider first the temperature dependence of the maximum gap. $\Delta_{max}(T)$ is plotted as a function of reduced temperature in Figure 4.10. The results for six different strengths of interlayer tunneling are shown, as well as the traditional BCS curve [12], which is scaled in this plot by multiplying with the zero temperature value of $\Delta_{max}(T)$ when $T_J = 43.78meV$. In all cases considered, $\Delta_{max}(T)$ is flat at low temperatures and turns over smoothly such that $\Delta_{max}(T = T_c) = 0$, as expected. Note that as T_J is increased from $T_J = 0meV$, the value of $\Delta_{max}(T)$ increases slightly at all temperatures, until $T_J = 19.6meV$, after which point it begins to drop in magnitude. It is also interesting that for the highest value of interlayer tunneling ($T_J = 43.78meV$) and no in-plane pairing, the gap maximum falls exactly on top of the BCS s-wave curve. Generally, the behaviour of the maximum gap for all strengths of pair tunneling is much the same as the traditional BCS maximum gap, and as such cannot be responsible for the change in

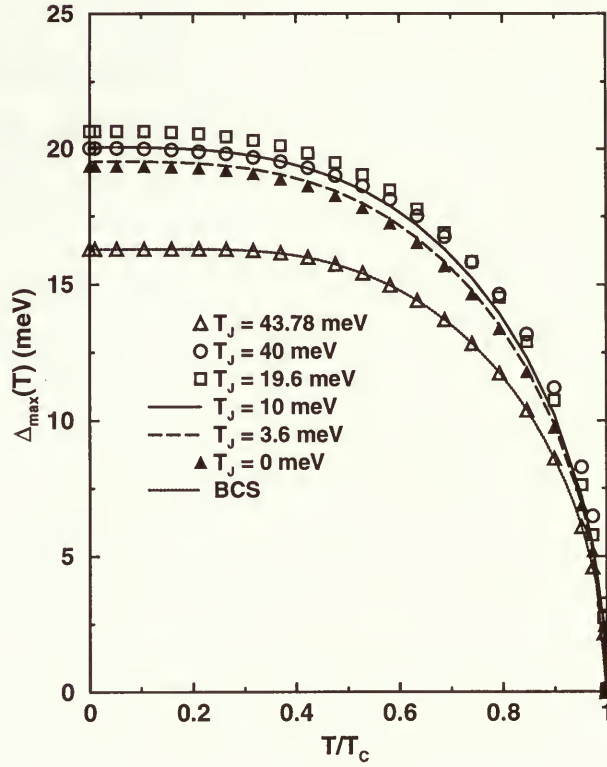


Figure 4.10: The maximum of the gap assuming d-wave BCS in-plane interaction for several strengths of interlayer tunneling.

curvature as T_J is increased.

In the original BCS theory, the maximum value of the gap at zero temperature is related to the critical temperature as

$$\frac{2\Delta_{max}(0)}{k_B T_c} = 3.53. \quad (4.1)$$

This is a universal number which does not depend on any interaction parameters, and can easily be used for comparison with experimental results. It is interesting to discover that the maximum value of the gap for no in-plane pairing is related to T_c in a similar manner as above. Consider first the gap given in Equation (2.38) for $V = 0 \text{ meV}$ and

$T = 0K$;

$$\Delta_{\mathbf{k}} = \sqrt{\left(\frac{T_J(\mathbf{k})}{2}\right)^2 - \varepsilon_{\mathbf{k}}^2 \Theta\left(\frac{T_J(\mathbf{k})}{2} - |\varepsilon_{\mathbf{k}}|\right)}, \quad (4.2)$$

where the step function is included to ensure that the argument underneath the square root is not negative. Assuming that the maximum of the gap occurs on the Fermi line, such that $\varepsilon_{\mathbf{k}} = 0$, then

$$\Delta_{\mathbf{k},max}(0) = \left. \frac{T_J(\mathbf{k})}{2} \right|_{max}. \quad (4.3)$$

At the critical temperature T_c , the structure of the gap equation represents an eigenvalue problem;

$$\Delta_{\mathbf{k}} = T_J(\mathbf{k}) \frac{1}{2|\varepsilon_{\mathbf{k}}|} \tanh\left(\frac{\varepsilon_{\mathbf{k}}}{2k_B T_c}\right) \Delta_{\mathbf{k}}. \quad (4.4)$$

For small x , the function $\tanh(x) \rightarrow x$, therefore as $\varepsilon_{\mathbf{k}} \rightarrow 0$ as it approaches the Fermi line, the above equation simplifies to

$$2k_B T_c = \left. \left(\frac{T_J(\mathbf{k})}{2}\right) \right|_{max}. \quad (4.5)$$

Finally, combining Equations (4.3) and (4.5), one finds that

$$\frac{2\Delta_{max}(0)}{k_B T_c} = 4, \quad (4.6)$$

so that the same ratio in the ILPT model with $V = 0$ is also a universal number independent of the interlayer tunneling strength! Furthermore, the zero temperature result obtained in the present research for the maximum gap with $T_J = 0meV$ confirms this result, yielding a ratio of 3.99. The consistency in the analytical and computational results of $\Delta_{max}(0)$ suggests that in the present research, the calculations of the maximum gap are accurate.

To investigate further the cause of the change in curvature of $1/\lambda^2(T)$ as T_J increases, consider again the momentum dependence of $\phi(\mathbf{k})$. Figures 4.8 and 4.11 show the gap for a large interlayer tunneling strength of $T_J = 40meV$ and for temperatures of $T = 0K$

and $T = 93K$. Clearly at zero temperature, the gap is finite along much of the Fermi line. However, at $T = 93K$, the gap is nearly zero everywhere and contains only rather sharp peaks at points on the Fermi line near the edge of the FBZ. Consequently, as temperature is increased, fewer and fewer \mathbf{k} points pick up finite contribution from $\phi(\mathbf{k})$. Recalling that $E(\mathbf{k}) = \varepsilon_{\mathbf{k}}$ when $\phi(\mathbf{k}) = 0$, clearly the paramagnetic term in $1/\lambda^2(T)$ quickly approaches the value of the diamagnetic term, diminishing the diamagnetic contribution over much of the momentum space. Because $1/\lambda^2(T)$ decreases quickly at low temperatures and must go to zero at $T = T_c$, the curve begins to “pull up”, giving rise to a convex shape

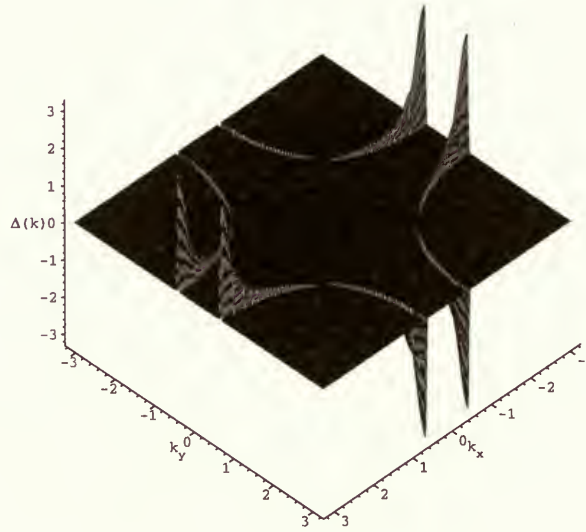


Figure 4.11: The structure of $\phi(\mathbf{k})$ in the BCS limit assuming d-wave symmetry of the in-plane interaction. Here, $T = 93K$ and $T_J = 40meV$.

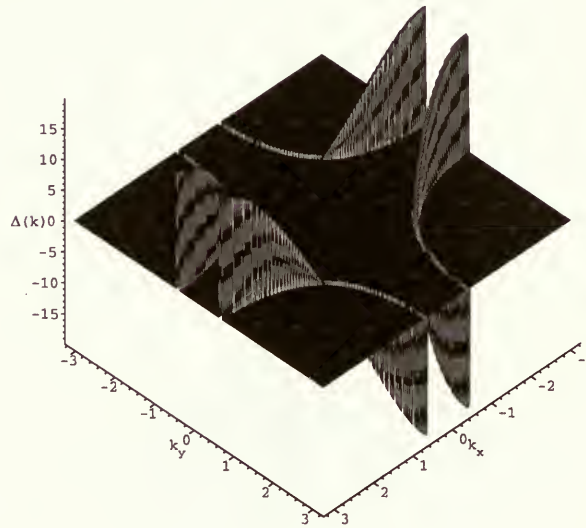


Figure 4.12: The structure of $\phi(\mathbf{k})$ in the BCS limit assuming d-wave symmetry of the in-plane interaction. Here, $T = 0K$ and $T_J = 0meV$.

of the penetration depth curve.

The situation is altered, however, when T_J is decreased and V is increased accordingly such that T_c is constant. Consider the gaps for $T_J = 0meV$ and $V = 2458.9meV$ at temperatures of $T = 0K$ and $T = 93K$ (Figures 4.12 and 4.13). The zero temperature gap is not much different in appearance from the gap at $T_J = 40meV$ in Figure 4.8. However, there is a striking difference in appearance of the gap at $T = 93K$. Here, $\phi(\mathbf{k})$ is still finite at many \mathbf{k} points along the Fermi line, and the sharp peaks which were observed in the case of $T_J = 40meV$ and $V = 783.2meV$ are not present here. As a result,

the gap more strongly influences the paramagnetic part of $1/\lambda^2(T)$ and the diminishing effect is not as great as temperature increases. This is why the shape of $1/\lambda^2(T)$ does not drop off quickly at low temperatures and is concave for smaller strengths of pair tunneling and finite in-plane interaction.

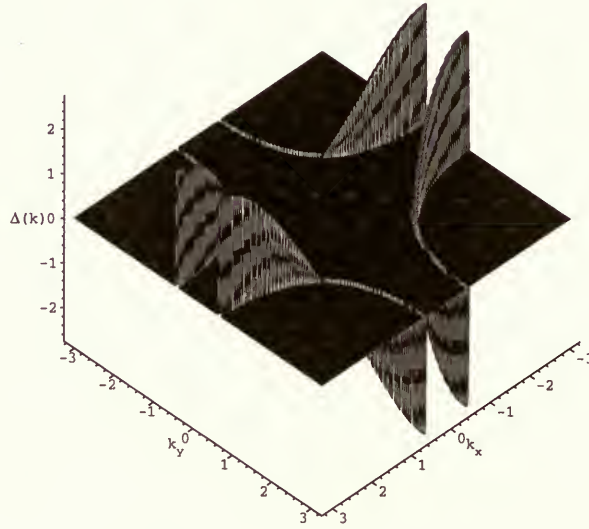


Figure 4.13: The structure of $\phi(\mathbf{k})$ in the BCS limit assuming d-wave symmetry of the in-plane interaction. Here, $T = 93K$ and $T_J = 0meV$.

As in the s-wave BCS limit, the difference between the two methods by which the penetration depth is calculated is considered in the d-wave case. Figure 4.14 illustrates this difference for interlayer tunneling strengths of $T_J = 0meV$ and $T_J = 40meV$. The direct \mathbf{k} summation method yields slightly lower values than the tetrahedron method

in the mid to high temperature range for both T_J values. The discrepancy is more pronounced when the interlayer tunneling is turned on. At low temperatures, $1/\lambda^2(T)$ continues to increase for direct \mathbf{k} summation, as was observed in the s-wave BCS limit. Again, the results below approximately 30% of T_c in the direct \mathbf{k} summation method are not trusted. Nevertheless, the two methods validate each other above this temperature and increase the confidence in the results of this work, since two completely different approaches give nearly identical results.

If an even larger lattice size is used for the calculations, it is found that the difference

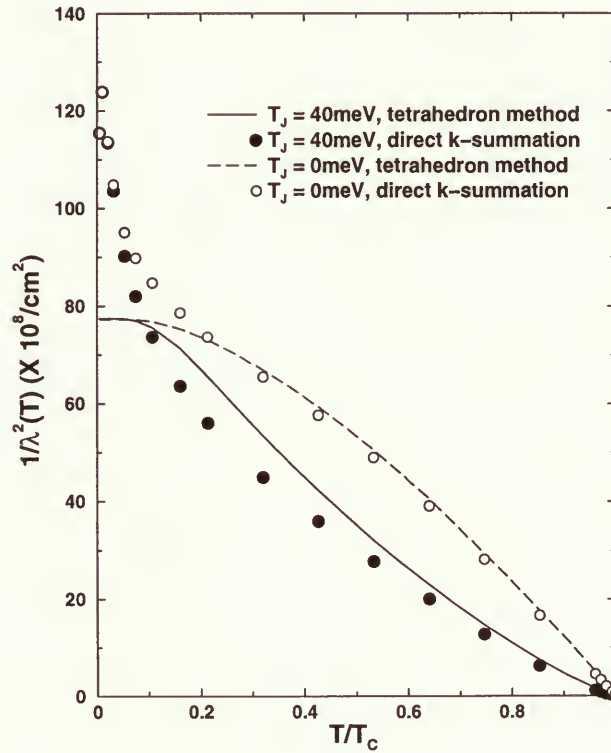


Figure 4.14: Comparison of $1/\lambda^2(T)$ calculated using the tetrahedron method and direct \mathbf{k} space summation assuming d-wave BCS in-plane interaction.

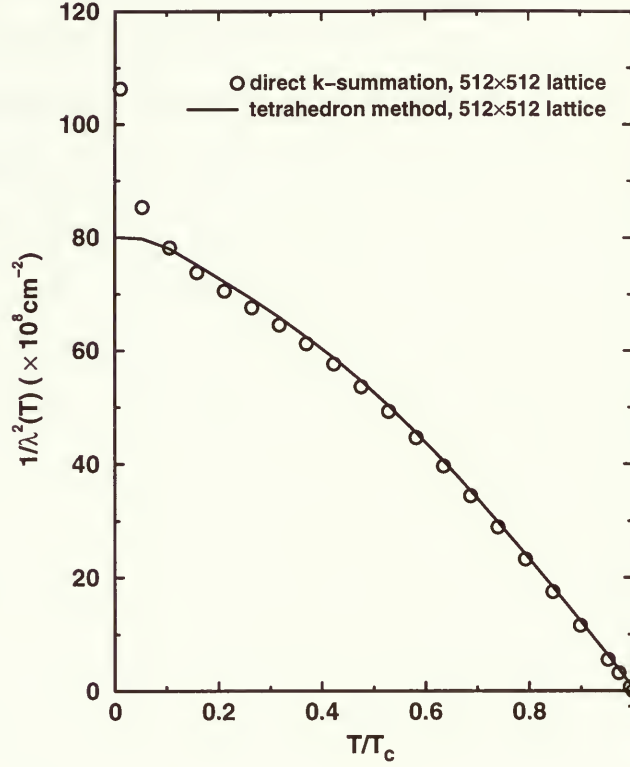


Figure 4.15: Comparison of $1/\lambda^2(T)$ calculated using the tetrahedron method and direct \mathbf{k} space summation for a 512×512 lattice assuming d-wave BCS in-plane interaction and no interlayer pair tunneling.

between the two methods is less obvious. This point is illustrated in Figure 4.15, where $1/\lambda^2(T)$ is plotted for a 512×512 lattice and the interlayer pair tunneling is turned off. The two curves are nearly identical and the \mathbf{k} summation values do not deviate from the results of the tetrahedron method until below $\approx 15\%$ of the critical temperature. The effect of the lattice size is clearly important in the computations here.

To investigate the role of lattice size in the calculations for the tetrahedron method, consider Figure 4.16 which presents the penetration depth calculations in the d-wave limit for the two extreme T_J values and for two different values of N . Note that the curves

are plotted down to 20% of T_c only, since the low temperature values have been ignored due to the numerical difficulties discussed earlier. Clearly for both $T_J = 0\text{meV}$ and $T_J = 40\text{meV}$, the effect of increasing the lattice size is to *suppress* the value of $1/\lambda^2(T)$. This seems reasonable considering that the paramagnetic contribution to the penetration depth diminishes the constant temperature independent contribution of the diamagnetic part of the current density. A larger lattice would mean that the paramagnetic term (which depends on $\phi(\mathbf{k})$) would have finite contributions from more \mathbf{k} points, making its magnitude larger in absolute value and more accurate than that calculated for a smaller lattice. Consequently, the diminishing effect of the paramagnetic contribution is greater for a larger lattice and the penetration depth curve is suppressed.

4.1.3 Knight Shift

The temperature dependence of the Knight shift was also investigated in this work, in light of the results for the penetration depth, which proved contradictory to the claim in [4] that the interlayer pair tunneling must be the dominant pairing mechanism in these materials. The Knight shift is calculated by Sudbø *et al.* [3] using a pair tunneling strength of $T_J = 43\text{meV}$ and an in-plane pairing cutoff of $\omega_D = 20\text{meV}$, assuming s-wave symmetry of the gap. They plot $K(T)/K(T_c)$ for two different values of in-plane interaction, $V = 244.2\text{meV}$ and $V = 488.4\text{meV}$, and for both a zero and finite Fermi liquid correction factor, $U = 0\text{meV}$ and $U = 2t = 500\text{meV}$. Sudbø *et al.* also include a calculation with d-wave symmetry of the gap, but they do not calculate the gap self consistently, and use instead the form $\Delta_{\mathbf{k}}^d(T) = \Delta_0^d(T)[\cos(k_x a) - \cos(k_y a)]/2$, with $2\Delta_0^d/T_c = 8$. This estimate of the ratio is very large compared to the usual mean field value of $2\Delta_0^s/T_c = 3.53$, and Sudbø *et al.* claim that the high value is justified because of small scattering and fluctuation effects in these materials, as was also discussed by Scalapino [14]. The results of Sudbø *et al.* for the Knight shift assuming this d-wave

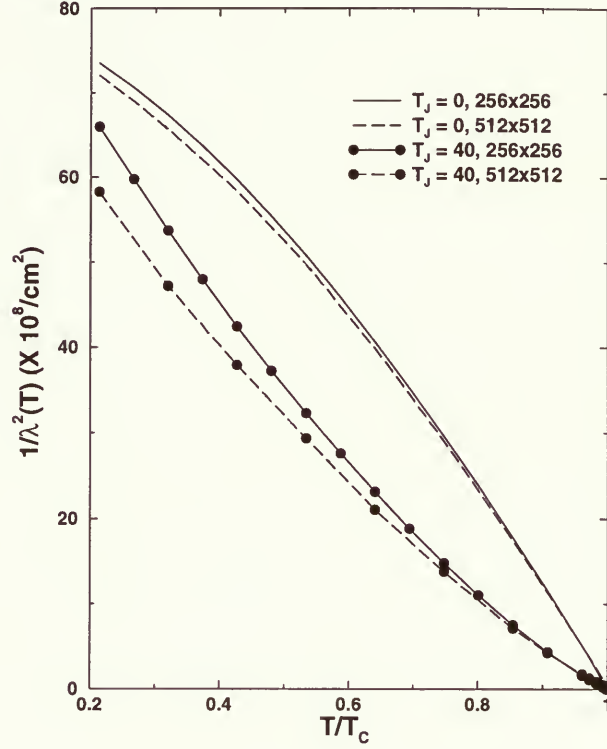


Figure 4.16: The effect of lattice size on $1/\lambda^2(T)$ calculated with the tetrahedron method assuming d-wave BCS in-plane interaction.

symmetry of the gap give good qualitative agreement with experiments, however, they note that the large value of $2\Delta_0^d/T_c = 8$ is responsible for “compressing” the curves such that they approach the curve of the experiments.

In this study the temperature dependence of the Knight shift is calculated according to Equation (2.65) by using the self consistent solutions for the gap for both the s-wave and d-wave cases. Consider first the s-wave scenario, for which $K(T)/K(T_c)$ is calculated using direct \mathbf{k} summation, and for the same parameters as those in [3]. The critical temperature is $T_c = 93.66K$ for $V = 244.2meV$, and $T_c = 100.2K$ for $V = 488.4meV$.

The results in Figure 4.17 are in good agreement with those presented by Sudbø *et al.* The open and filled diamonds represent the experimental results [15, 16] for an applied field parallel and perpendicular, respectively, to the sample. The best agreement with the experimental points is found for higher in-plane interaction, $V = 488.4meV$, and stronger Fermi liquid corrections, $U = 500meV$.

Figure 4.18 shows the Knight shift results for d-wave symmetry, where V varies such that T_c is constant at $94.55K$. The calculations are performed using the direct \mathbf{k} summation approach on a 512×512 lattice with the strength of the Fermi liquid corrections

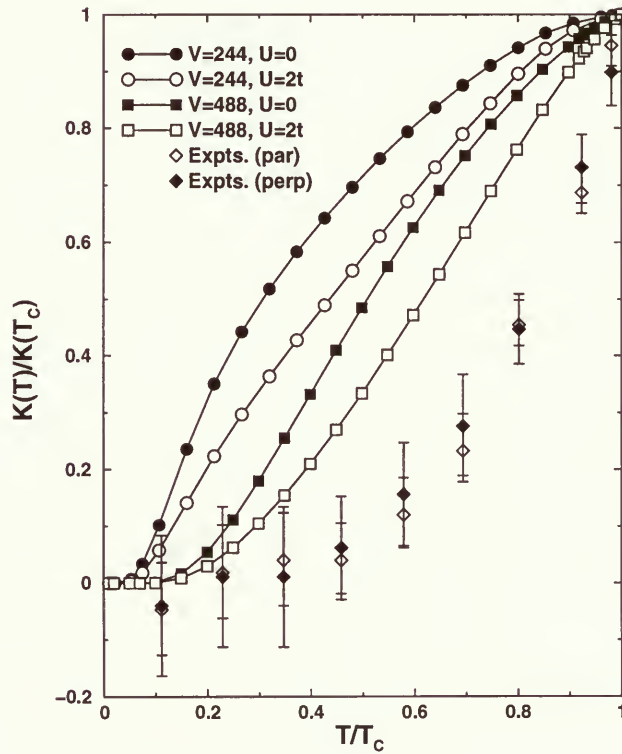


Figure 4.17: The Knight shift calculated for $T_J = 43meV$ assuming s-wave BCS in-plane interaction.

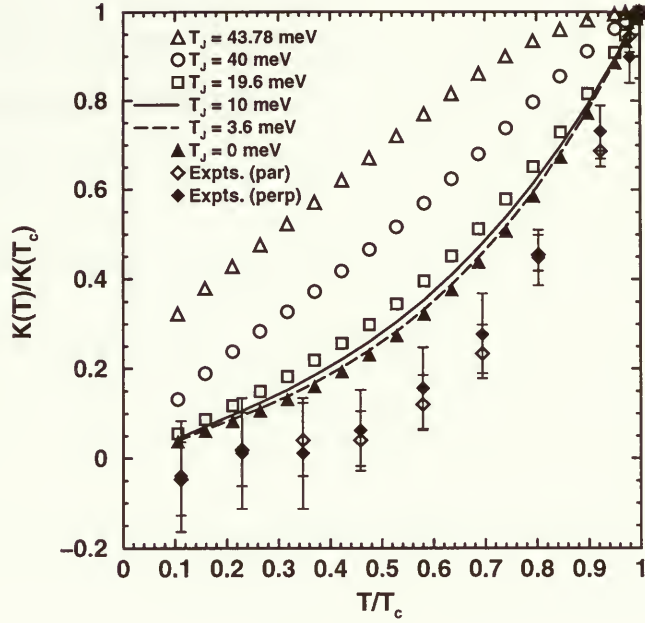


Figure 4.18: The Knight shift calculated for several different strengths of pair tunneling assuming d-wave BCS in-plane interaction.

set to $U = 500 \text{ meV}$, as in [3]. Note that the results of the calculations for temperatures less than $10\%T_c$ have not been included. At these lowest temperatures, the results were again hindered by limitations in the numerical method, and thus only the results which are reliable are presented.

As in the case of the penetration depth calculations, it is clear that an increase in T_J causes a substantial change in the curvature of $K(T)/K(T_c)$. For small strengths of pair tunneling, as well as for $T_J = 0 \text{ meV}$, $K(T)/K(T_c)$ is in reasonable agreement with the experimental points, and shows the same overall curvature. However, when

T_J is increased to strengths greater than $\approx 20meV$, such that T_J dominates over the in-plane pairing, the curvature of $K(T)/K(T_c)$ looks nothing like experiments. Once again, the findings reveal no evidence that the interlayer tunneling mechanism must be the dominant pairing mechanism in order to obtain results in good qualitative agreement with experiments.

4.1.4 Neutron Scattering Intensity

Neutron scattering experiments on optimally doped YBCO [17, 18] show a distinct magnetic feature in the superconducting state near the wave vector $\mathbf{Q} = (\pi/a, \pi/a, \pi/c_b)$ and at an energy of $41meV$. Yin *et al.* [4] recently calculated the neutron scattering intensity, and they claim that the ILPT model can explain the appearance of this sharp feature. They emphasize that the gap must have $d_{x^2-y^2}$ symmetry, and that the interlayer pair tunneling must be the dominant pairing mechanism in these high T_c materials in order to explain the the magnetic neutron peak which is observed in experiments.

In light of the present research results for the penetration depth, which give curves nothing like experiments when the pair tunneling dominates, this research can be extended further by calculating the neutron scattering intensity within the ILPT formalism in the BCS limit. The calculations of $\text{Im}\chi(\mathbf{q}, \omega)$ were performed using the tetrahedron method applied to Equation (2.68), where $\mathbf{q} = \mathbf{Q}$ as in [4]. $\text{Im}\chi(\mathbf{Q}, \omega)$ is calculated at zero temperature for a 1024×1024 lattice, assuming d-wave symmetry of the gap. Several strengths of interlayer tunneling are considered, and the in-plane interaction is cutoff at $\Omega_D = 20meV$. As in the case of the penetration depth, the magnitude of the in-plane pairing interaction V is varied such that the critical temperature is kept constant. Here, the critical temperature is $T_c = 94.55K$.

The results for the neutron scattering intensity are shown in Figure 4.19. All of the results show a strong magnetic feature in $\text{Im}\chi(\mathbf{Q}, \omega)$, and as T_J is increased this feature

shifts to lower energies. For small strengths of interlayer pair tunneling, the neutron peak occurs at approximately $35\text{--}43\text{meV}$, which lies in the neighborhood of the peak at 41meV seen in the experiments. The peaks for small T_J are considerably broader than those found for large T_J . Also included in the plot are the results of the calculation of $\text{Im}\chi(\mathbf{Q},\omega)$ in the pure BCS limit with a d-wave gap given by $\Delta_{\mathbf{k}} = (\Delta_{\text{max}}/2)[\cos(k_x a) - \cos(k_y a)]$ for all \mathbf{k} in the FBZ, where $\Delta_{\text{max}} = 25\text{meV}$ [4] (see the dot-dashed line in Figure 4.19). This case was also considered by Yin *et al.* [4], and in the present work this calculation was performed as a check to ensure that in fact this result could be reproduced. In this case there is a step discontinuity at approximately 41meV , and no peak is observed. It is interesting that this calculation with $T_J = 0\text{meV}$ and the above form of the gap gives no peak, while the present research result for $T_J = 0\text{meV}$ calculated with the self consistent d-wave gap solutions and $\Omega_D = 20\text{meV}$ shows a distinct peak in the vicinity of the experimental peak. Clearly the form of the gap is important here and one cannot simply assume an arbitrary model for $\Delta_{\mathbf{k}}$ without solving self consistently for the gap below the critical temperature.

The reason for the discrepancy between the plots for nonzero T_J in the present study and those of Yin *et al.* [4] is not entirely clear. Their curves are very smooth and show none of the noise observed in the present work, and they make no mention of the size of the lattice used in their calculations. Furthermore, all curves here (with the exception of the pure BCS limit given by the dot-dashed line) exhibit a “shoulder” at the onset of the magnetic peak, a feature which is not found in the plots presented by Yin *et al.* They argue that a large value of interlayer tunneling ($T_J = 75\text{meV}$) is required in order for $\text{Im}\chi(\mathbf{Q},\omega)$ to exhibit the magnetic feature found in experiments. It seems that, based on the present study’s results for $\text{Im}\chi(\mathbf{Q},\omega)$, a high strength of interlayer tunneling (i.e. $T_J \geq 40\text{meV}$) is not necessary to capture the feature observed in experiments, but rather that a small strength of T_J , or even $T_J = 0\text{meV}$, leads to a neutron peak in the vicinity

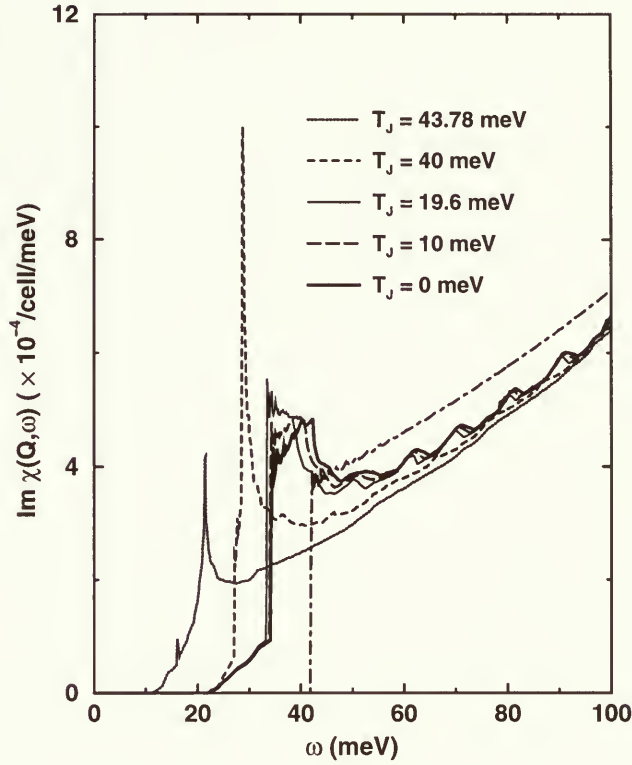


Figure 4.19: The magnetic neutron scattering intensity at $T = 0K$ for several strengths of interlayer pair tunneling and $\Omega_D = 20meV$.

of the experimentally observed peak. Furthermore, when T_J dominates, the calculations show a peak that is very sharp in energy, while the experiments [17, 18] indicate that the peak is broader, on the order of 15–20 meV in width. Again, the present research results for moderate to small T_J values are in better agreement in this respect with the experiments than the results where the pair tunneling is the dominate pairing mechanism.

To be thorough, the calculation of $\text{Im}\chi(\mathbf{Q}, \omega)$ was also performed in this work with an increased in-plane interaction cutoff, such that Ω_D is increased from 20 meV to 200 meV. As noted at the beginning of this Chapter, Yin *et al.* [4] do not mention the value of

Ω_D in their work, so it is therefore important to investigate the effect of a large cutoff in addition to the original cutoff of $\Omega_D = 20meV$. An increase in Ω_D effectively means that the gap will be finite over a larger width $2\hbar\Omega_D$ around the Fermi line.

The results are shown in Figure 4.20, where again, V is varied such that $T_c = 94.55K$. For $T_J = 43.78meV$, there is no change in $\text{Im}\chi(\mathbf{Q}, \omega)$ for increased Ω_D , since this largest T_J value corresponds to zero in-plane pairing. For the next smaller strength of pair tunneling, $T_J = 40meV$, the peak is slightly larger in this high Ω_D limit, and the “shoulder” at the onset of the peak is nearly disappeared. In fact, this feature is not found in any of the finite in-plane pairing curves for $\Omega_D = 200meV$. The most notable effect of increasing the in-plane pairing cutoff, however, is a smearing of the neutron peak for smaller pair tunneling strengths. Both the height and width of the peaks are suppressed for large Ω_D . Clearly the peaks in this limit are not as well defined as for $\Omega_D = 20meV$. These results seem to suggest that in order to capture the features of the experiments, the interaction must be cutoff at a fairly narrow region around the Fermi line, and that the gap cannot be finite over too large a width as it is with a large cutoff Ω_D .

It must be noted also at this stage that both the penetration depth and the Knight shift were recalculated using this increased in-plane interaction cutoff, $\Omega_D = 200meV$, for $T_J = 0meV$, $T_J = 19.6meV$, and $T_J = 40meV$. In all cases the results were nearly identical to those obtained for the original cutoff of $\Omega_D = 20meV$. To understand this behaviour, consider that both the expressions for $1/\lambda^2(T)$ and $K(T)$ depend on the factor $-\frac{\partial f(E)}{\partial E}$, which is a sharply peaked function around the Fermi line. Because this factor effectively disregards any finite contribution of the gap $\phi(\mathbf{k})$ outside a width of $k_B T$ around the Fermi line, the increase in Ω_D does not affect the results. Furthermore, the structure of the gap in the region which does contribute is largely determined by the form of the pair tunneling term $T_J(\mathbf{k})$, as well as the in-plane pairing kernel $V_{\mathbf{k},\mathbf{k}'}$.

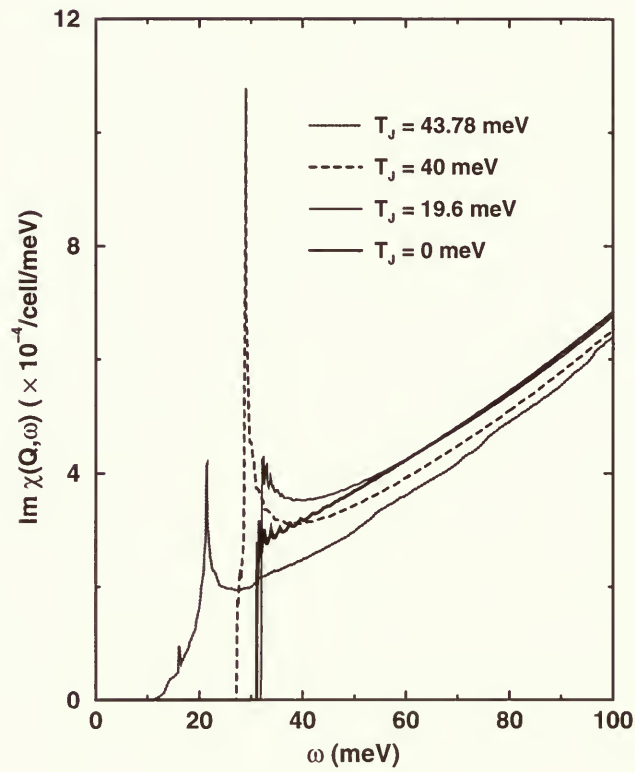


Figure 4.20: The magnetic neutron scattering intensity at $T = 0K$ for several strengths of interlayer pair tunneling and an increased in-plane cutoff of $\Omega_D = 200 \text{ meV}$.

4.2 Strong Coupling Limit

For the case of in-plane pairing due to spin fluctuations there are a number of parameters that are required by the program. As in the BCS limit, the band parameters are $t = 250\text{meV}$ and $t'/t = -0.45$. The band filling factor n was set to 0.75 electrons of spin up and spin down per cell, and the chemical potential μ varied so that n remained constant during the iterative procedure discussed in Chapter 2. The cutoff frequency was set at $\omega_c = 6000\text{meV}$, which is three times the bandwidth, and the parameters of the spectral function $P(\Omega)$ were $\omega_{max} = 400\text{meV}$ and $\omega_0 = 8\text{meV}$. The critical temperature in the strong coupling calculations was kept constant at $T_c = 91.57\text{K}$.

As discussed in Section 3.2.1, the penetration depth in the strong coupling limit was calculated using both the direct \mathbf{k} summation and tetrahedron methods. Recall that in addition to the self consistent solutions in the superconducting state, the normal state solutions below T_c are also required to calculate $1/\lambda^2(T)$ in this limit (see Equation(2.53)). However, great difficulties were encountered when attempting to iterate self consistently for these normal state solutions (Equations (2.24) and (2.25) with $\phi(\mathbf{k}, i\omega_n) = 0$). The solutions for $Z^N(\mathbf{k}, i\omega_n)$ and $\chi^N(\mathbf{k}, i\omega_n)$ did not converge to a sufficient accuracy regardless of the number of iterations performed.

Fortunately, it was possible to take advantage of the fact that the diamagnetic contribution to the penetration depth is a constant, as discussed in Section 2.4.2. Using this idea, one need only iterate for the solutions $Z(\mathbf{k}, i\omega_n)$, $\chi(\mathbf{k}, i\omega_n)$, and $\phi(\mathbf{k}, i\omega_n)$ in the superconducting state, all of which converged with relative ease. Once these solutions are obtained, it is straightforward to calculate the paramagnetic contribution to the penetration depth by considering the first term only in Equation (2.53). Recalling that the contribution from this term is negative, it then follows that the value of the diamagnetic contribution has exactly the same magnitude as the paramagnetic contribution at

T_c , but with opposite sign, such that $1/\lambda^2(T = T_c) = 0$. Thus, once the paramagnetic contribution had been determined, the value of the diamagnetic contribution was determined by the condition that the penetration depth be infinite as the material reverts back into the normal state at T_c was satisfied. The validity of this was confirmed in the BCS limit, where the diamagnetic contribution was easily calculated separately from the paramagnetic contribution, and the two were found to contribute exactly equal and opposite amounts at the critical temperature. The diamagnetic contribution was also calculated separately for all temperatures below T_c , and was found to be independent of temperature as expected. This simplification was made in the calculation of $1/\lambda^2(T)$ for both the \mathbf{k} summation and tetrahedron methods. A quadratic fit was used with the calculated paramagnetic contribution at the three highest temperatures considered to determine the constant diamagnetic contribution, with the requirement that the fitted value of $1/\lambda^2(T)$ vanish at $T = T_c$. The coefficient of the quadratic term in the fit was two to three orders of magnitude smaller than the coefficient of the linear term.

Consider first the penetration depth calculated using the tetrahedron method with a 64×64 lattice. $1/\lambda^2(T)$ was calculated for three different strengths of pair tunneling, and the curves are given in Figure 4.21. For all three T_J values, the shape of $1/\lambda^2(T)$ is completely inconsistent with experiments (see Figure 1.2). While small strengths of pair tunneling in the BCS limit yielded results with the correct overall curvature, it is found here that the convex nature is present for all strengths of T_J . Not only is the curvature incorrect, but the results for $1/\lambda^2(T)$ are significantly smaller in magnitude than those obtained in the weak coupling limit (see Figure 4.5). Note also that the results are shown only down to a temperature of $\approx 44\%$ of the critical temperature. The quantities $Z(\mathbf{k}, i\omega_n)$, $\chi(\mathbf{k}, i\omega_n)$, and $\phi(\mathbf{k}, i\omega_n)$ could not be determined below $T = 40K$ because of the computer memory limitations. Recall that for the strong coupling calculations, the number N_c of Matsubara frequencies is a function of temperature, where

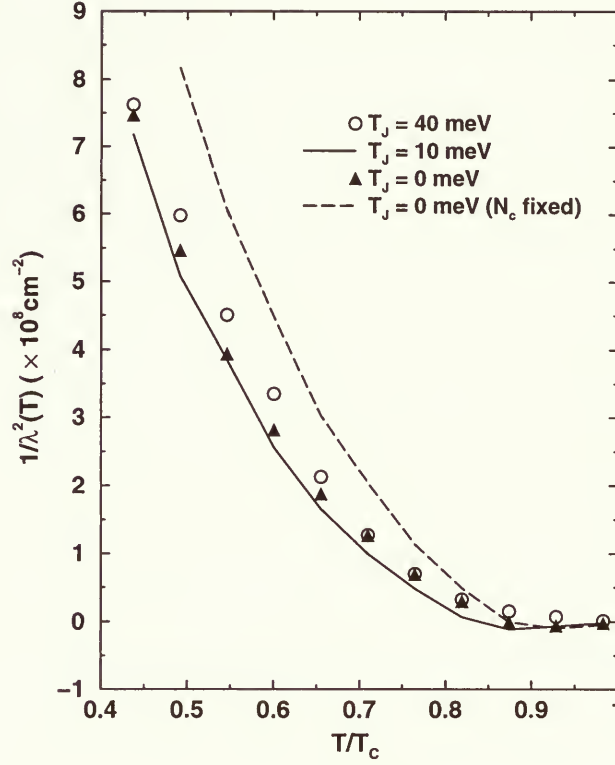


Figure 4.21: $1/\lambda^2(T)$ calculated in the strong coupling limit using the tetrahedron method.

$N_c = [\omega_c/(2\pi T) + 0.5]$. Thus, as temperature is decreased, the number of frequencies over which the sums in Equations (2.24), (2.25), (2.26), and (2.53) are performed increases. Below $T/T_c = 0.44$, the memory requirements of the program were beyond the capacity of the available computing system.

To investigate whether the changing number of Matsubara frequencies affects the results, the calculation of $1/\lambda^2(T)$ for no pair tunneling was also considered with a fixed number of frequencies (given by the dashed line in Figure 4.21). The cutoff ω_c was varied such that N_c was constant at 280. There is a small improvement in the results since the

magnitude of $1/\lambda^2(T)$ increases slightly, but the curvature remains essentially unchanged.

Figure 4.22 shows the results of the calculations using the direct \mathbf{k} summation approach. There is little difference between these results and those in Figure 4.21. Direct \mathbf{k} summation yields results for $1/\lambda^2(T)$ which are slightly less in magnitude than the tetrahedron method values, with the exception of the $T_J = 40\text{ meV}$ case, where it is found that the \mathbf{k} summation values are slightly higher. Despite these small differences, the overall agreement between the two methods confirms the results of this work for $1/\lambda^2(T)$ in the strong coupling limit. Clearly the temperature dependence of the penetration depth cannot be reproduced in this limit for any strength of pair tunneling.

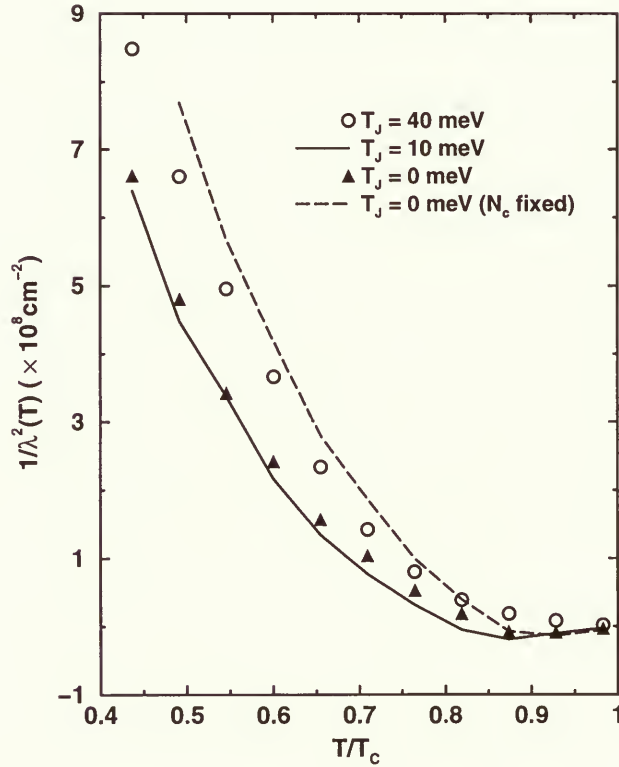


Figure 4.22: $1/\lambda^2(T)$ calculated in the strong coupling limit using direct \mathbf{k} summation.

In this strong coupling limit, it is believed that the limitations on the lattice size and the energy cutoff ω_c affect the accuracy of the results. Because the maximum lattice size which can be considered is 64×64 , $1/\lambda^2(T)$ does not pick up contributions from enough \mathbf{k} points, and consequently is drastically undervalued. More importantly, the limited number of Matsubara frequencies over which the sums are performed also contributes to the problem. Note that the relation given in Equation (2.55) is strictly speaking only valid if the sum over n runs from $-\infty \rightarrow n \rightarrow \infty$, so it is expected that the truncation of the sum will introduce an error in the results. Throughout the course of this strong coupling research, it was necessary to continually alter the parameters N_c , N , and ω_c with temperature such that the memory requirements did not exceed the capacity of the system. Because the calculations could not be performed with a lattice larger than 64×64 , or for greater than a few hundred Matsubara frequencies, no comment can be made on the minimum lattice size needed to yield reasonable values of $1/\lambda^2(T)$, nor on whether the curvatures would be improved if either N or N_c were increased.

As in the BCS limit, it is instructive to examine the structure of the gap to try to further understand the behaviour of $1/\lambda^2(T)$ in the strong coupling limit. In this case, the gap is given as $\Delta(\mathbf{k}, i\omega_n) = \phi(\mathbf{k}, i\omega_n)/Z(\mathbf{k}, i\omega_n)$, such that the quantity $\phi(\mathbf{k}, i\omega_n)$ is renormalized. Note that in the BCS limit, the retardation effects associated with spin fluctuation mediated pairing are absent, and thus the gap in the BCS case is simply $\phi(\mathbf{k})$, which is synonymous with $\Delta(\mathbf{k})$.

Figures 4.23 and 4.24 show the gap at the first Matsubara frequency for $T_J = 40\text{meV}$ and temperatures of $T = 40\text{K}$ and $T = 90\text{K}$, respectively. Note the striking difference between these gaps compared to those presented in the BCS limit. It is clear in the strong coupling limit that the small lattice size causes the gap to be very jagged in nature, and none of the smoothness which was evident in the BCS limit is present. At $T = 90\text{K}$, the gap is finite only over a limited region of the FBZ, and its maximum value is

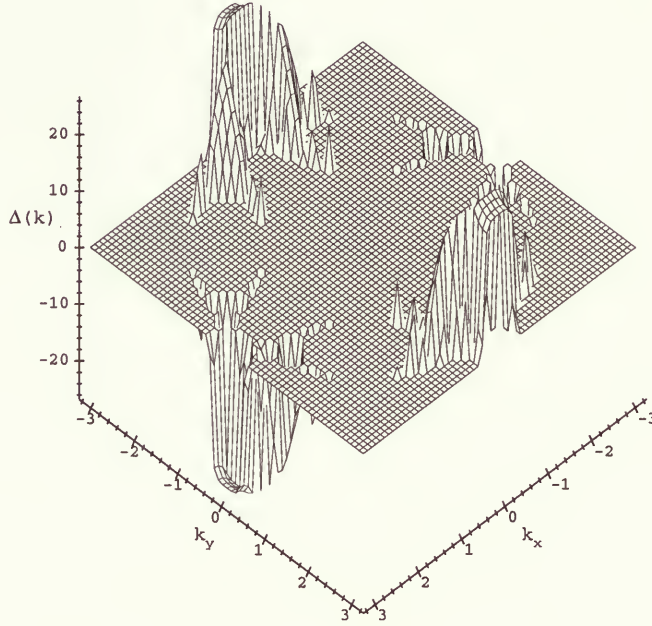


Figure 4.23: The structure of the gap at the first Matsubara frequency. Here, $T_J = 40\text{meV}$ and $T = 40\text{K}$.

approximately a third of the maximum value at $T = 40\text{K}$, the lowest temperature which could be considered. At $T = 40\text{K}$, the gap is somewhat smoother in appearance and is finite at more \mathbf{k} points than at higher temperature. This same general temperature dependence is also observed for $T_J = 0\text{meV}$, for which the gap at both $T = 40\text{K}$ and $T = 90\text{K}$ is plotted in Figures 4.25 and 4.26, respectively. Again, a decrease in temperature increases the overall size of the gap, and $\Delta(\mathbf{k}, i\omega_n = 1)$ is finite for more \mathbf{k} points in the FBZ at lower temperatures. Note also that in this strong coupling limit,

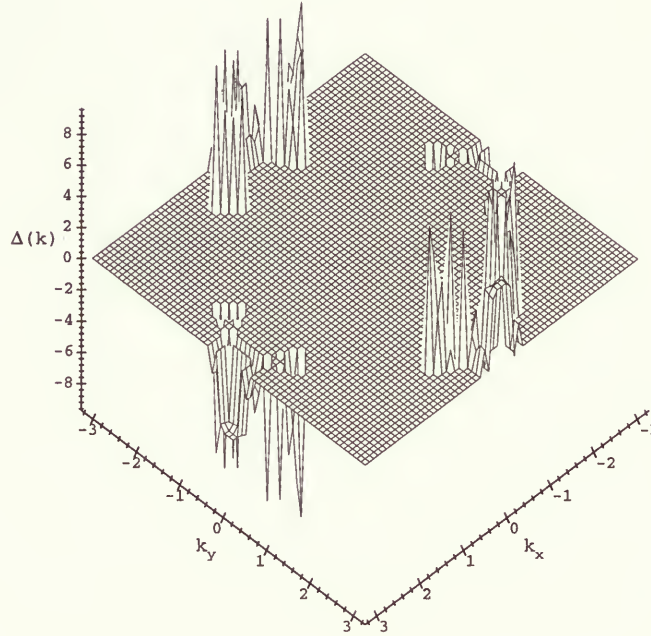


Figure 4.24: The structure of the gap at the first Matsubara frequency. Here, $T_J = 40\text{meV}$ and $T = 90\text{K}$.

the dependence of the gap on the strength of interlayer tunneling is not as great as in the BCS limit, and consequently there is not a considerable amount of difference between the penetration depth curves for different T_J values. All of the curves obtained in the present strong coupling research have a convex shape because there is not enough contribution to $1/\lambda^2(T)$ from the gap due to the limited size of the lattice, as well as the limited number of Matsubara frequencies.

For completeness, plots showing the structure of the functions $Z(\mathbf{k}, i\omega_n)$ and $\chi(\mathbf{k}, i\omega_n)$

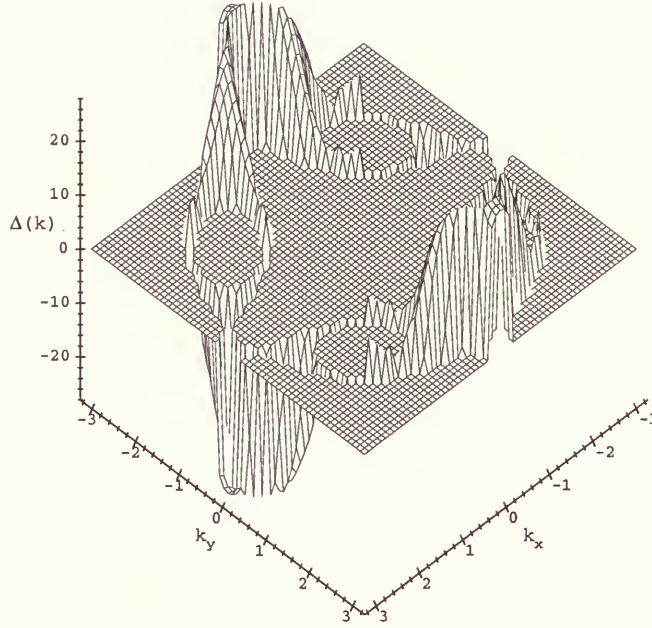


Figure 4.25: The structure of the gap at the first Matsubara frequency. Here, $T_J = 0\text{meV}$ and $T = 40\text{K}$.

at the first Matsubara frequency are also included in this work. Figures 4.27 and 4.28 show $Z(\mathbf{k}, i\omega_n = 1)$ for temperatures of $T = 40\text{K}$ and $T = 90\text{K}$, where $T_J = 40\text{meV}$, and Figures 4.29 and 4.30 show $\chi(\mathbf{k}, i\omega_n = 1)$ for the same parameters, respectively. As in the case of the gap, the effect of the limited lattice size is clearly evident in the jagged nature of both $Z(\mathbf{k}, i\omega_n = 1)$ and $\chi(\mathbf{k}, i\omega_n = 1)$. The structure of these functions, together with the structure of $\Delta(\mathbf{k}, i\omega_n)$ and a small number of Matsubara frequencies, cause the results for $1/\lambda^2(T)$ in this work to be both underestimated and incorrectly shaped.

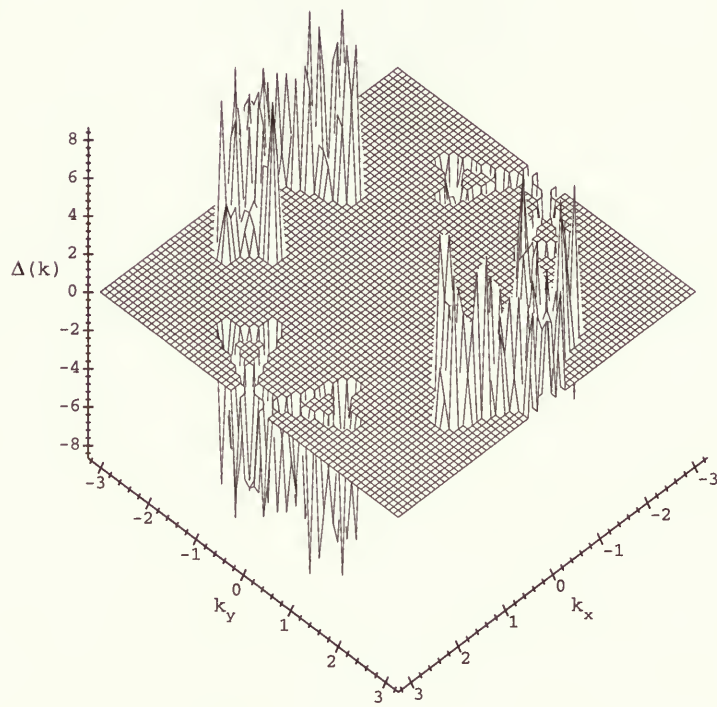


Figure 4.26: The structure of the gap at the first Matsubara frequency. Here, $T_J = 0 \text{ meV}$ and $T = 90 \text{ K}$.

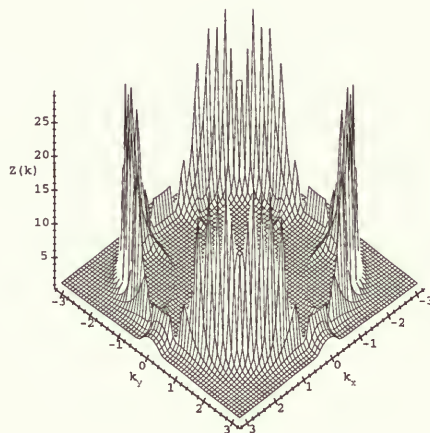


Figure 4.27: The structure of $Z(\mathbf{k})$ at the first Matsubara frequency. Here, $T_J = 40 \text{ meV}$ and $T = 40 \text{ K}$.

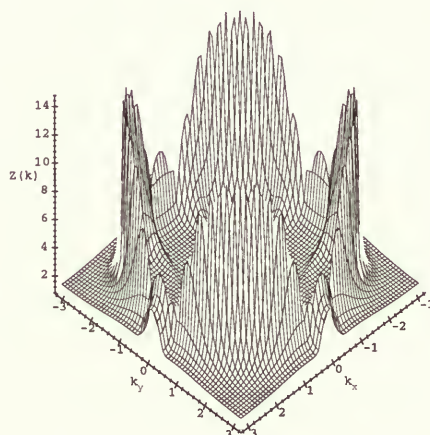


Figure 4.28: The structure of $Z(\mathbf{k})$ at the first Matsubara frequency. Here, $T_J = 40 \text{ meV}$ and $T = 90 \text{ K}$.

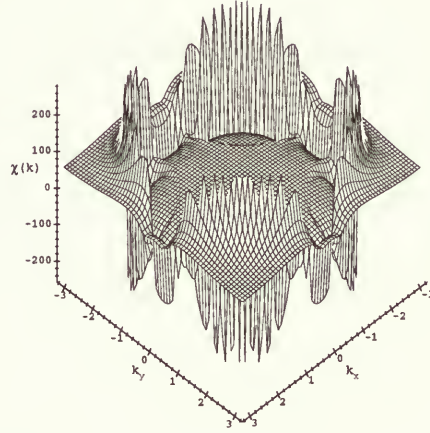


Figure 4.29: The structure of $\chi(\mathbf{k})$ at the first Matsubara frequency. Here, $T_J = 40\text{meV}$ and $T = 40\text{K}$.

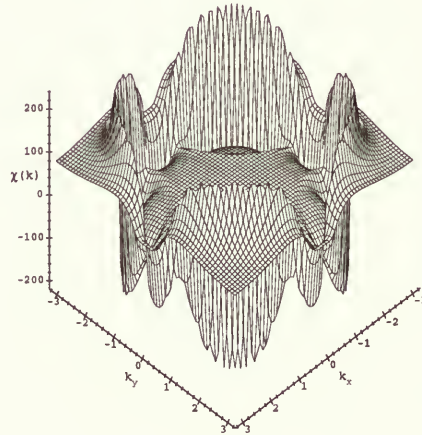


Figure 4.30: The structure of $\chi(\mathbf{k})$ at the first Matsubara frequency. Here, $T_J = 40\text{meV}$ and $T = 90\text{K}$.

Chapter 5

CONCLUSIONS

This thesis has focused on the calculation of the magnetic field penetration depth within the formalism of the Interlayer Pair Tunneling Model of Chakravarty *et al.* [1]. The main goal of the research was to investigate the extent to which the ILPT model could reproduce the experimental results for the penetration depth in the high temperature cuprate superconductor $\text{YBa}_2\text{Cu}_3\text{O}_{7-x}$. To make the study as comprehensive as possible, several different models of in-plane pairing interaction were considered. These were BCS s-wave pairing, BCS d-wave pairing, and spin fluctuation interactions.

In the weak coupling BCS limit, it was found that the interlayer pair tunneling suppressed the penetration depth curves for both the s-wave and d-wave scenarios. For s-wave in-plane pairing interaction, the $1/\lambda^2(T)$ curves for small strengths of pair tunneling looked like the usual BCS result, and increasing T_J resulted in a gradual lowering of this curve. The highest T_J value considered was $T_J = 40\text{meV}$, and here the shape of the penetration depth curve was convex with respect to the origin, with no resemblance to that found in experiments (Figure 1.2).

The same general trends were true in the d-wave BCS limit, shown in Figure 4.5, but $1/\lambda^2(T)$ was nearly linear at low temperatures down to approximately $T/T_c = 0.15$, at which point the curves flattened due to the numerical procedures involved with the tetrahedron method. If the values in this $0-0.15T/T_c$ range are ignored, the behaviour of $1/\lambda^2(T)$ for small interlayer tunneling ($0 \leq T_J \leq 20\text{meV}$) looks qualitatively like the experimental results. Again, when T_J dominates, the curves have a shape which is

nothing like those of the experiments.

Furthermore, a comparison was made between the two methods by which the penetration depth was calculated in the s-wave and d-wave BCS limits. The tetrahedron and \mathbf{k} summation methods produced consistent results in the mid to high temperature ranges, but deviated at low temperatures. The \mathbf{k} summation results were not trustworthy below about 30% of T_c , at which point they began to deviate from the tetrahedron method results. The flattening of $1/\lambda^2(T)$ observed for d-wave in-plane interaction using the tetrahedron method suggests that the values below 15% of T_c should be disregarded for this case. For both methods used, these uncharacteristic results at very low temperatures are not physically relevant, but rather it appears that they are strictly due to the numerical methods themselves.

The maximum value of the gap was also determined and the usual BCS curve was found to lie exactly on top of the $\Delta_{max}(T)$ curve when $T_J = 43.78meV$ and $V = 0meV$. $\Delta_{max}(T)$ for all values of T_J was flat at low temperatures and closely resembled the usual temperature dependence of the BCS maximum gap, suggesting that the convex curvature of $1/\lambda^2(T)$ for large T_J is not a consequence of some peculiar behaviour in $\Delta_{max}(T)$. Furthermore, it was shown that the ILPT model predicts a universal number for the ratio

$$\frac{2\Delta_{max}(0)}{k_B T_c} = 4 \quad (5.1)$$

when there is no in-plane interaction present.

The present research also considered briefly the calculation of the Knight shift in the weak coupling limit. In the s-wave scenario, the results were in agreement with those in [3] for $T_J = 43meV$, and the closest agreement to experiments was found for high in-plane interaction, $V = 488.4meV$, and large Fermi liquid corrections $U = 500meV$. However, for the d-wave case, the results suggested that small strengths of interlayer

pair tunneling yield results closer to the experiments, as was clear in Figure 4.18. The results, which were obtained using the self consistent solutions for the gap, were in good qualitative agreement with the experimental points using small to moderate strengths of pair tunneling ($0 \leq T_J \leq 20meV$). $K(T)/K(T_c)$ plotted as a function of reduced temperature for large strengths of pair tunneling showed an incorrect curvature.

Finally, this research looked at the neutron scattering intensity in the weak coupling limit with d-wave in-plane interaction. Peaks in the intensity were found for all strengths of T_J and coincided most closely to the experimental peak at $41meV$ when T_J was small. When T_J dominated, the peak was very sharp and occurred at a lower energy than the peak for modest T_J . There was no evidence in the calculations to suggest that a large strength of pair tunneling is necessary to obtain a peak in $\text{Im}\chi(\mathbf{Q},\omega)$. The importance of using the self consistent gap solutions was especially evident in this case, since the simple form for $\Delta_{\mathbf{k}}$ assumed by Yin *et al.* did not produce a peak in $\text{Im}\chi(\mathbf{Q},\omega)$ when $T_J = 0meV$. After performing the same calculations with an increased cutoff Ω_D and the self consistent d-wave gap solutions, it was found that the peaks for smaller strengths of pair tunneling were not as pronounced, which led to the conclusion that the in-plane interaction must be finite only over a narrow width off the Fermi line.

Throughout the course of this work, it became increasingly apparent that the size of the lattice in momentum space plays a crucial role in the accuracy of the calculations. It was found that for all quantities calculated in this work, it was essential to always use as large a lattice as possible so that contributions from many \mathbf{k} points are taken into account in the sums over momenta. In the BCS limit, a minimum lattice size of 256×256 was necessary to yield reliable results, and the results for all quantities considered were improved even further for 512×512 and 1024×1024 lattices.

The effect of a finite lattice size was especially limiting in the strong coupling case,

for which the largest size considered was a 64×64 lattice because of the sums over Matsubara frequencies. The results for $1/\lambda^2(T)$ were undervalued for both the \mathbf{k} summation and tetrahedron methods in comparison to the BCS results, and displayed a curvature which was completely inconsistent with the experimental results for both large and small strengths of pair tunneling. It is believed that the reason for this behaviour is due to both the limited number of Matsubara frequencies and to the jagged nature of the functions $Z(\mathbf{k}, i\omega_n)$, $\chi(\mathbf{k}, i\omega_n)$, and $\phi(\mathbf{k}, i\omega_n)$, which is a consequence of the limited number of \mathbf{k} points.

In summary, it is stressed that the results found in this research for the penetration depth, Knight shift, and neutron scattering intensity are inconsistent with the notion that the interlayer pair tunneling must be the dominant pairing mechanism in order to obtain results in agreement with experiments. It is found that for small strengths of pair tunneling, such that $0 \leq T_J \leq 20meV$, the overall features of the experiments are captured reasonably well. The calculations in this work do not discount the Interlayer Pair Tunneling model completely, but rather show that this tunneling mechanism cannot be the dominant pairing mechanism in $YBa_2Cu_3O_{7-x}$, and that the in-plane interaction also plays an important role in these high- T_c materials.

Bibliography

- [1] S. Chakravarty, A. Sudbø, P.W. Anderson, and S. Strong, *Science* **261**, 337 (1993).
- [2] B. Mitrović and M. Castle, *J. Phys.: Condens. Matter* **9**, 9007 (1997).
- [3] A. Sudbø, S. Chakravarty, S. Strong, and P.W. Anderson, *Phys. Rev. B* **49**, 12245 (1994).
- [4] L. Yin, S. Chakravarty, and P.W. Anderson, *Phys. Rev. Lett.* **78**, 3559 (1997).
- [5] J.D. Jorgensen, B.W. Veal, A.P. Paulikas, L.J. Nowicki, G.W. Crabtree, H. Claus, and W.K. Kwok, *Phys. Rev. B* **41**, 1863 (1990).
- [6] W.N. Hardy, D.A. Bonn, D.C. Morgan, R. Liang, and K. Zhang, *Phys. Rev. Lett.* **70**, 3999 (1993).
- [7] O.K. Andersen, A.I. Liechtenstein, O. Jepsen, and F. Paulsen, *J. Phys. Chem. Solids* **56**, 1573 (1996).
- [8] V.N. Kostur and B. Mitrović, *Phys. Rev. B* **51**, 6064 (1995).
- [9] A.C. Rose-Innes and E.H. Rhoderick, *Introduction to Superconductivity, 2nd Edition* (Pergamon Press Ltd., Exeter, 1978).
- [10] J.R. Schrieffer, *Theory of Superconductivity* (W.A. Benjamin, Inc., New York, 1964).
- [11] G. Lehmann and M. Taut, *Phys. Status Solidi b* **54**, 469 (1972); *Phys. Status Solidi b* **57**, 815 (1973).
- [12] B. Mühschlegel, *Zeitschrift für Physik* **155**, 313 (1959).

- [13] D.N. Basov, R. Liang, D.A. Bonn, W.N. Hardy, B. Dabrowski, M. Quijada, D.B. Tanner, J.P. Rice, D.M. Ginsberg, and T. Timusk, *Phys. Rev. Lett.* **74**, 598 (1995).
- [14] D.J. Scalapino, *J. Phys. Chem. Solids* **54**, 1433 (1993).
- [15] M. Takigawa, P.C. Hammel, R.H. Heffner, Z. Fisk, K.C. Ott, and J.D. Thompson, *Physica* **162-164**, 853 (1989).
- [16] M. Takigawa, P.C. Hammel, R.H. Heffner, and Z. Fisk, *Phys. Rev. B* **39**, 7371 (1989).
- [17] F.H. Fong, B. Keimer, P.W. Anderson, D. Reznik, F. Doğan, and I.A. Aksay, *Phys. Rev. Lett.* **75**, 316 (1995); F.H. Fong, B. Keimer, D. Reznik, D.L. Milius, and I.A. Aksay, *Phys. Rev. B* **54**, 6708 (1996).
- [18] P. Bourges, L.P. Regnault, Y. Sidis, and C. Vettier, *Phys. Rev. B* **53**, 876 (1996).

